Acta Materialia 277 (2024) 120190

Contents lists available at ScienceDirect

Acta Materialia

journal homepage: www.elsevier.com/locate/actamat

Critical impacts of thermodynamic instability and short-range order on deformation mechanisms of VCoNi medium-entropy alloy

T.H. Chou [a], W.P. Li [a,b,c,*], L.Y. Zhu [a], F. Zhu [a,c], X.C. Li [a,c], J. Huang [a,d], Y.X. Wang [e], R. Zhou [a], W.Y. Chen [a], J.H. Luan [a], Y.L. Zhao [e], Z.X. Wu [a], F.R. Chen [a,c,*], J.C. Huang [a], P.K. Liaw [f], X.L. Wang [g], T. Yang [a,*]

[a] Department of Materials Science and Engineering, City University of Hong Kong, Kowloon, Hong Kong, China
[b] Beijing Institute of Nanoenergy and Nanosystems, Chinese Academy of Sciences, Beijing, China
[c] Time-resolved Aberration Corrected Environment (TRACE) Electron Microscope Unit, City University of Hong Kong, Kowloon, Hong Kong, China
[d] State Key Laboratory of Powder Metallurgy, Central South University, Changsha, China
[e] School of Materials Science and Engineering, Harbin Institute of Technology (Shenzhen), Shenzhen, China
[f] Department of Materials Science and Engineering, University of Tennessee, Knoxville, USA
[g] Department of Physics and Center for Neutron Scattering, City University of Hong Kong, Kowloon, Hong Kong, China

ARTICLE INFO

Keywords:
Multi-principal element alloys
Short-range order
Thermal stability
Stacking fault energy

ABSTRACT

Short-range order (SRO) has made a splash in the recent research on multi-principal element alloys (MPEAs), among which the equiatomic VCoNi alloy was regarded as the most potential prototype. However, in addition to disputes over SRO, there is still a lack of agreements on the phase stability and deformation mechanism of the VCoNi alloy, which should be addressed before the SRO can be independently analyzed. To this end, microstructural evolutions with increasing long-term annealing temperatures (from 700 to 1,200 °C) were first inspected in detail to determine critical temperatures for phase transitions unambiguously. Our results revealed that the VCoNi alloy was still dominated by the face-centered-cubic (FCC) structure with a minor κ phase at 900 °C and became a single FCC solid solution at above 910 °C. Subsequently, by carefully examining dislocation configurations and stacking fault (SF) widths in the FCC phases annealed at 900 °C and 1,200 °C, significant variations in local stacking fault energy (SFE) were unveiled, and the overall SFE decreased with increasing annealing temperature. Combined with the state-of-the-art density function theory (DFT)-based lattice Monte Carlo (MC) simulation, we demonstrated how the rise/decline in SFE can be explained by the greater/lower degree of SRO. This research would not only offer new perspectives for recent controversies over phase stability, deformation mechanism, and SRO characterization technique using electron diffraction but also shed light on the intrinsic relationship between SRO and local stacking fault energy of MPEAs.

1. Introduction

Single-phase MPEAs, including high/medium entropy alloys (HEAs/MEAs), have received both technological and scientific attention not only as a consequence of their unprecedented mechanical and functional properties but also because of understanding the underlying formation mechanism of solid solutions to facilitate alloy design [1–6]. They, at one time, had been studied as ideal (random) complex concentrated solid solutions stabilized by the high configurational entropy [7,8]. However, later investigations disclosed that other phases or local chemical ordering at the Angstrom scale arose from the preferential pairing of constituent elements, *i.e.*, SRO, could form in these single-phase MPEAs that were thought to be thermodynamically stable [9–11]. For example, secondary phases were observed in the equiatomic CrCoNiFeMn HEA (Cantor alloy), the very first prototype of single-phase FCC MPEAs, after prolonged annealing at intermediate temperatures [12–15], driving the materials community to carefully evaluate the phase stability of other MPEAs that appear to be single-phase solid solutions. The equiatomic CrCoNi MEA, on the other hand, is unambiguously a single-phase FCC solid solution, while recent theoretical calculations and experiments suggested that SROs evolve at intermediate temperatures due to energetically favorable Cr–Co and Cr–Ni

* Corresponding authors at: Department of Materials Science and Engineering, City University of Hong Kong, Kowloon, Hong Kong, China.
E-mail addresses: liwanpeng@binn.cas.cn (W.P. Li), frchen@cityu.edu.hk (F.R. Chen), taoyang6-c@my.cityu.edu.hk (T. Yang).

https://doi.org/10.1016/j.actamat.2024.120190
Received 24 January 2024; Received in revised form 11 July 2024; Accepted 12 July 2024
Available online 17 July 2024

bindings within the alloy [16–21]. For the same reason, the nature of chemical complexity seemingly makes SRO a universal yet non-neglectable feature of MPEAs [22–25]. Subsequently, it was increasingly reported that SROs could affect or explain, in varying degrees, the physical and mechanical properties of MPEAs, but most relevant topics are still in the early stages and under debate [10,11, 26–31]. More clear evidence correlating the SRO with specific properties is still needed.

Unlike detectable and visible long-range-order secondary phases (typically at least a few nanometer-sized), experimentally demonstrating SROs in MPEAs (primarily focusing on FCC solid solutions containing 3d elements) heavily relies on advancements in theory and instrument [10,11]. Prevailing methods used to monitor the development of SROs in conventional binary alloys for decades, including X-ray/neutron diffraction (particularly by X-ray absorption spectroscopy) [32], electron diffraction [33], and electrical resistivity measurement [34], encounter their difficulties to various extents when it comes to describing SROs in MPEAs. With increasing alloying elements, interpreting the diffuse scattering of X-rays/neutrons could be more demanding due to subtle discrepancies in atomic scattering factors of 3d elements, such as Cr, Co, and Ni [29], which requires high-quality beamline facilities and sophisticated data postprocessing [17,22,26,35, 36]. As for the electron diffraction using transmission electron microscopy (TEM), detected extra superlattice-like reflections (diffuse disks) were extensively reported in recent studies and attributed to the presence of SROs [20,21,24,27,37–39] despite little research questioning their validity [29,40,41]. Nevertheless, of the latest viewpoint, Walsh et al. systematically reviewed the possible origins of these reflections and pointed out that these reflections do not necessitate SROs in MPEAs [30]. Soon after, Coury et al. proved that most observed diffuse disks in literature could be unambiguously explained by diffraction effects from higher-order Laue zones [31]. In addition to the above popular approaches of all time, state-of-art techniques, such as the atomic-resolution elemental mapping, were employed but either limited [21,24,28,42] or at issue [10,31]. It should be noted that all methods above were frequently applied to further connect the existence of SRO with mechanical properties or deformation behaviors; however, the provided information may be insufficient. That is, aside from the respectful arguments over developing effective ways to detect the SROs, more than these characterizations revealing elemental or structural information is needed to elucidate how the SROs affect the deformation behaviors of MPEAs.

SFE could be a breakthrough in answering this question, which is a fundamental parameter reflecting deformation mechanisms of alloys, *e.g.*, dislocation mobility, twin ability, and phase stability. For the CoCrNi MEA, the most widely studied surrogate of SRO among MPEAs, early theoretical calculations commonly yielded negative values of SFEs from cryogenic to room temperatures [43–46] such as −3 mJ/m^2 at 27 °C according to the DFT calculation [44], which completely contradicts experimental values of 22 ± 4 [47] and 18 ± 4 [48] mJ/m^2 at room temperature by measuring the distances between partial dislocations in the weak-beam dark-field (WBDF) images. Considering that details could be missing in diffraction contrast images, Smith et al. took advantage of high-angle annular dark-field scanning transmission microscopy (HAADF-STEM) to unveil, at the atomic scale, a notable deviation of Shockley partials widths (or SFEs) in the Cantor alloy, and further suggested that similar variations in local SFEs can occur in other concentrated solid solutions [49].

Such speculation can be theoretically explained after the SRO was reconsidered in the CrCoNi MEA [16,18,50], but there is still a lack of agreement in experimental verifications [19,29]. According to DFT calculations, SFEs could considerably fluctuate between−140 to 65 mJ/m^2 with an average value of−42.9 mJ/m^2 in a disordered state. Moreover, the DFT-MC simulation indicated that the mean SFEs could be tunable by tailoring degrees of SRO, ranging from−42.9 to 30 mJ/m^2, while fluctuations in SFEs of all SRO states remain resembling [18]. With regard to experimental attempts, the SFE of the CrCoNi MEA was shown to substantially increase from 8 ± 1.43 mJ/m^2 in the disordered state to 23.33 ± 4.31 mJ/m^2 in an SRO state (annealing at 1000 °C for 120 h) [19]. However, a recent study argued that the SFE remained unchanged after the CrCoNi alloy was annealed at 500 °C for 168 h [29]. It seems that even if SFE could be controlled by various degrees of SROs, the sizeable change in SFE of the CrCoNi MEA was less than theoretical predictions and still inadequate to alter the deformation mechanism. In other words, deformation via SFs and deformation twinning (DT), as well as their relevant formation mechanisms, stayed unchanged. Additionally, some investigations are of the opinion that the strengthening effects of SROs on the mechanical properties of the CrCoNi MEAs, such as hardness, tensile strengths, and ductility, are rather limited [26–29]. This is not to say that the influences of SRO could be neglected in the CrCoNi MEA; instead, based on previous achievements, exploring more pronounced SROs in other MPEAs has become a top priority.

The equiatomic VCoNi MEA is, therefore, of great interest to the present work because of its stronger tendency to form SROs [24,51], as well as its superior mechanical and functional properties [52–57]. In the first instance, Sohn et al. demonstrated that among single-phase FCC MPEAs, the VCoNi alloy has the highest yield strengths with comparable ductility as well as the highest friction stress and Hall-Petch coefficient, which can be ascribed to the severe lattice distortion effect by ab initio calculations [52]. Later, SRO was also observed in the nearly equiatomic VCoNi alloy in the wake of preferential V–Co and V–Ni bindings [24]. Compared to Cr in the CrCoNi alloy, it can be expected that V induces more significant SRO in the VCoNi alloy due to higher negative mixing enthalpy, which can be seen from the fact that the phase decomposition of a single FCC phase into two intermetallic phases takes place at intermediate temperatures [54], while no secondary phase can form in the CrCoNi alloy over a wide temperature range, as mentioned above. Still, follow-up surveys are somehow absent, and SRO-related concerns of the VCoNi alloy urgently need to be clarified as follows: (1) Since SRO was introduced into the VCoNi alloy by annealing at 900 °C for merely 150 s [24] or at 880 °C for 180 s [37] (far less than the time adopted by investigations on the SRO of the CrCoNi MEA), it is necessary to examine the thermodynamic stability of SRO at particular temperatures by long-term annealing. (2) After such short-term annealing, the $L1_2$ phase with a volume fraction of ~ 20 % precipitated within the FCC matrix in addition to SRO [24]. It was argued that occurrences of SRO and long-range-order $L1_2$ precipitates at the same time would be unexpected [30]. (3) No known research has quantitatively revealed whether SROs have, and to what extent, impacts on the mechanical properties of the VCoNi alloy compared with that of other SRO-affected MPEAs. (4) Although the SFEs of the VCoNi alloy were theoretically calculated as low as ~ 30 mJ/m^2 at room temperature [56] and − 11 mJ/m^2 at−273 °C [46], neither of the two representative deformation structures of low SFE materials — DT and high-density SFs was found at room temperature and cryogenic temperatures [52–57]. Therefore, this study aims to comprehensively dig into these critical issues and explore whether the contradictions can be theoretically and experimentally explained after reevaluating the SRO.

In addition to the above issues on SROs, we notice that the literature about the phase stability and deformation mechanism of the VCoNi alloy is inconclusive and sometimes contradicting. At first sight, it was reported that the VCoNi alloy was purely a single FCC structure at 900 °C or above, which would decompose into σ + κ at 800 °C (eutectoid reaction) [54]. However, three different structures were reported at 900 °C, *i.e.*, FCC (annealing for 1 h) [54], FCC with SRO + $L1_2$ (annealing for 150 s) [24], and FCC + κ (annealing for 10 min) [58]. It is still unclear why the secondary $L1_2$ phase formed by short-term annealing will transform and then redissolve into the matrix with increasing annealing time. Even with the aid of CALPHAD (CALculation of PHAse Diagrams), the calculated phase diagrams apparently could not fully support experimental results [53–55]. Additionally, some studies claimed that planar slip is the predominant dislocation configuration due to severe

lattice distortion [52], while the other one suggested the dislocation tangle instead [24], which may be further linked to the influence of SFE. Thus, considering the promising mechanical and functional properties of the VCoNi alloy, as well as the increasing scientific interest in SRO, its temperature-dependent structural evolutions and associated deformation mechanisms will be comprehensively determined before proceeding to experimentally and computationally probe the impact of SRO on SFE.

In this work, the phase stability of the VCoNi MEA was studied by means of long-term annealing, followed by multiscale characterizations of each appeared phase and tensile testing. Then, the deformation mechanisms were elucidated by analyzing deformation microstructures in depth, especially for the specimen annealed at 900 °C. After that, we endeavored to estimate SFEs by examining the atomic structure of dislocations using HAADF-STEM. Moreover, first-principles DFT computations and MC simulations were performed, with the advanced consideration of the SRO parameter, to theoretically quantify the substantial effect of SRO on SFE in response to the experimental calculation.

2. Materials and methods

2.1. Sample preparation

The equiatomic VCoNi alloy was fabricated from pure elements (purities higher than 99.9 wt.%) via arc-melting under a high-purity argon atmosphere. Each button ingot was flipped and re-melted at least six times to ensure the macro-chemical homogeneity and then drop-casted into a copper mold with a dimension of 50 × 12 × 5 mm^3. The as-cast slabs were sealed in the evacuated and argon-backfilled quartz tubes and then homogenized at 1200 °C for 24 h, followed by water quenching. The homogenized slabs were subsequently rolled step by step at ambient temperature along the longitudinal direction to a total thickness reduction of 85 %. Finally, these cold-rolled sheets were sealed in the evacuated and argon-backfilled quartz tubes again and then annealed at 700 °C, 800 °C for 336 h, 840 °C, 850 °C, 860 °C, 870 °C, 900 °C, 1000 °C for 168 h, and 1200 °C for 24 h, respectively, followed by water quenching. For convenience, the specimens are hereafter referred to as A700, A800, A840, A850, A860, A870, A900, A1000, and A1200, respectively, according to their last annealing temperatures. In light of the long-term annealing, the microstructures of alloys were presumed to be close to equilibrium. Working temperatures of the muffle furnaces were strictly corrected with external thermocouples before each heat treatment to ensure that the temperature error of the sample place does not exceed ± 5 °C.

2.2. Microstructural characterization

The global composition of the as-cast ingots was analyzed by the inductively coupled plasma atomic emission spectroscopy (ICP-AES, Thermo Fisher Scientific). Phase identifications were performed by an X-ray diffractometer (XRD, SmartLab 9 kW, Rigaku) with Cu-Kα radiation at 40 kV. The specimens for the XRD analysis were prepared by mechanical grinding with SiC abrasive papers (grit sizes up to 4000) and subsequent mechanical polishing with ~50 nm SiO_2 suspension. The scanning rate was set to 5°/min with a scanning step size of 0.02°

Further microstructural characterizations were conducted by using electron backscattering diffraction (EBSD, Symmetry S2, Oxford), TEM (JEM-2100F, and JEM-ARM300F2, JEOL), and atom probe tomography (APT, LEAP 5000 XR, CAMECA). The EBSD characterizations were carried out on a field-emission scanning electron microscope (FE-SEM, Supra 55, Zeiss) equipped at an accelerating voltage of 15 kV. Specimens for the EBSD characterizations were mechanically ground, polished, and then further electrochemically polished in a mixed solution of HNO_3: C_2H_5OH = 1:9 (volume ratio) at 20 V/− 30 °C. As for the TEM characterizations, diffraction contrast images, including bright-field, dark-field, and selected area electron diffraction (SAED) patterns, were acquired by using JEM-2100F, while the Cs-corrected JEM-ARM300F2 was employed to obtain atomic-resolution HAADF-STEM images (with inner and outer collection semi-angles of 71.3 and 180 mrad, respectively). To prepare TEM samples, the sheets were firstly mechanically ground to ~ 45 μm using SiC abrasive papers, punched to round discs with 3 mm in diameter, dimpled to a thickness of ~ 10 μm using Gatan 656, and finally ion-milled to a thickness of electron transparency using Gatan PIPS 695. In the case of the APT characterization, the specimens were analyzed in a voltage mode at 70 K, with a pulse repetition rate of 200 kHz, a pulse fraction of 20 %, and an evaporation detection rate of 0.3 % atom per pulse. The 3D reconstructions and data analysis were conducted using Imago Visualization and Analysis Software (IVAS) version 3.8. Needle-shaped specimens were fabricated by lift-outs and annular milling in a focused ion beam/scanning electron microscope (FIB/SEM, Scios, FEI).

2.3. HAADF-STEM image processing and simulation

To reduce the noise and amorphized background of the atomic-resolution HAADF-STEM images, some images were processed by band-pass and wiener filtering [59]. The geometrical phase analysis (GPA) was conducted using the FRWRtools plugin, implemented in the DigitalMicrograph software [60]. Structural modeling, SAED pattern simulations, and HAADF-STEM image simulations were performed using VESTA, TEMPAS, and QSTEM [61], respectively. The microscope parameters for the simulations are described as follows: high voltage = 300 kV; defocus = 0; astigmatism = 0; spherical aberration = 0; temperature = 300 K; chromatic aberration = 1.6 mm (standard value of ARM300F2); thermal diffuse scattering (TDS) runs 30 times; the convergence semi-angle of the electron probe and the collection semi-angles are the same as that adopted in the experiment.

2.4. Mechanical testing

Flat dog-bone-shaped specimens with a gauge dimension of 12.5 × 3 × 0.75 mm^3 for the uniaxial tensile testing were sectioned by electro-discharge machining along the rolling direction of the sheets. Uniaxial room-temperature tensile tests were conducted at a strain rate of $1 \times 10^{-3}\ s^{-1}$ on a universal testing machine (Instron 3228) with a 10-mm extensometer attached.

2.5. Computational methods

Spin-polarized DFT calculations were performed using the Vienna Ab initio Simulation Package (VASP) [62,63]. The exchange and correlation interaction energies were determined through the generalized gradient approximation (GGA) with Perdew-Burke-Ernzerhof (PBE) parameterization [64]. The valence states of each element are detailed in **Table S1**, with core electrons being substituted by projector augmented wave (PAW) pseudopotentials [65]. To expedite the MC simulations, the total energy was computed at a plane-wave kinetic energy cutoff of 350 eV, and the convergence was attained when the energy variation dropped below 10^{-5} eV/atom in consecutive electronic iterations. The Monkhorst-Pack k-grid was employed to sample the Brillouin zone with the smallest k-point spacing set at 0.3 $Å^{-1}$.

The MC simulations were employed to investigate how the atom site occupancy evolves as the system approaches thermodynamic equilibrium configurations at 1173 K and 1473 K. The process began by creating a periodic 4 × 4 × 4 FCC supercell using lattice parameters derived from XRD results. The lattice was then populated with nominally equal atomic fractions in a special quasirandom structure (SQS) [66] generated using the alloy theoretic automated toolkit (ATAT) package [67]. During each MC step (i), the total energy of the current configuration was calculated as U_i in VASP. Then, a pair of atoms of different species were randomly selected and swapped. The total energy of the new configuration was computed as U_{i+1}. The swap was accepted

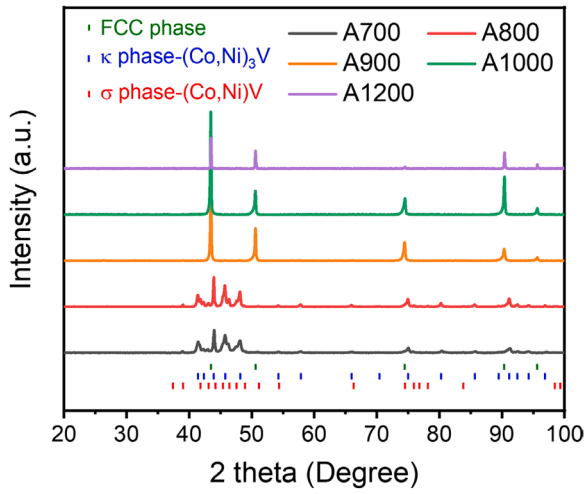

Fig. 1. XRD profiles of the equiatomic VCoNi alloys after different annealing processes.

with a probability, P_i, based on the Metropolis-Hastings algorithm [68]:

$$P_i = \min\left\{1,\ \exp\left(-\frac{U_{i+1} - U_i}{kT}\right)\right\} \quad (1)$$

where k is the Boltzmann constant, and T is the thermodynamic temperature. The convergence for MC simulations were assumed when the energy variation dropped below 5 meV/atom within 1000 MC steps, as shown in **Fig. S1**. During the simulation, static calculation was done for each swap of atom types, and full relaxation (both atoms and box) was done at the end of the MC runs.

2.6. Short-range parameter

The degree of the chemical ordering around an atom of the constituent element can be quantified by the Warren-Cowley parameter [16,18,50]:

$$\alpha_{ij}^{s} = 1 - \frac{p_{ij}^{s}}{c_j} \quad (2)$$

where p_{ij}^{s} is the probability of element j at the s_{th} nearest neighbor (NN) shell of element i, and c_j is the molar fraction of element j. α_{ij}^{s} (α_{VV}^{1}, α_{VCo}^{1}, α_{VNi}^{1}, *etc.*) = 0 represents no binding tendency; the positive/negative value is parallel to a tendency of the unfavored/favored *i*–*j* pairing, *i.e.*, *j* is unfavorable/favorable at the s_{th} NN site of *i*.

3. Results

3.1. Phase identification of the VCoNi MEA after long-term annealing

The ICP-AES results reveal that the actual composition of the homogenized VCoNi ingot is $V_{32.89}Co_{33.30}Ni_{33.81}$ (at.%), which is very close to the nominal equiatomic composition. The XRD spectrums of the A700, A800, A900, A1000, and A1200 samples are shown in Fig. 1. Obviously, the characteristic FCC peaks can only be identified at temperatures above 900 °C, and the A700 and A800 samples are dominated by the κ phase ($Co_{37.5}Ni_{37.5}V_{25}$; ICSD database code: 102,597) and σ phase ($V_{62}Co_{38}$; ICSD database code: 102,717), which all seems to be consistent with the previous results [54]. The lattice parameters of phases are summarized in Table 1. The κ phase is a close-packed ordered nine-layer rhombohedral phase with a space group of R-3m and a stacking sequence of abcbcacab [54,69,70], which is stable when the atomic ratio of Co and Ni is between 3:2 and 1:4 [71]. To facilitate the description of the crystal geometry, the rhombohedral κ phase here is indexed by hexagonal unit cells. The $V_{62}Co_{38}$ σ phase is a topologically close-packed phase with a space group of $P4_2/mnm$ [72]. Further detailed analyses of the κ and σ phases will be given in Section 4.2.

3.2. Multiscale microstructural characterizations of the VCoNi MEA after long-term annealing treatment

More microstructural information on the long-term annealed samples was unraveled by EBSD, TEM, and APT characterizations, as shown in **Figs. S2–4** and Figs. 2–4. Since the A700 and A800 samples have the same phase components (κ and σ) and similar microstructures (**Fig. S2** and Fig. 2, respectively), for simplicity and clarity, the A800 will be representatively discussed in the following content. The EBSD mappings of the A800 sample (Fig. 2**(a)–(c)**) clearly reveal a eutectoid structure comprising a matrix of the κ phase with the minor σ phase inside grains (smaller elongated particles or lamellae) and at grain boundaries (larger particles), agreed by further TEM evidence (Fig. 2**(d)–(g)**). The crystallographic structures of the κ matrix and σ particles in the TEM BF image (Fig. 2**(d)**) can be confirmed by the corresponding indexed SAED patterns (Fig. 2**(e)** and Fig. 2**(f)**, respectively). Interestingly, high-density planar defects are also found in the BF image of the κ phase (Fig. 2**(d)**), which can be referred to as the twinning diffraction spots (circled in cyan) and the streaks (pointed by yellow arrows) in the SAED pattern of the κ phase (Fig. 2**(f)**), indicating the co-existence of twin boundaries and SFs along the (0001) basal plane. For clarity, the DF image (Fig. 2**(g)**) is applied to highlight the high-density annealing nano-twins in the κ matrix.

In addition to the structural information, the elemental analysis of the dual-phase microstructure is displayed in the HAADF-STEM image

Table 1
Phase constituents and associated lattice parameters, chemical compositions, and volume fraction in the VCoNi alloys after long-term isothermal treatments at various temperatures.

Alloys	Phase	Lattice parameter (Å)	Composition (at.%)			Volume fraction (%)
			V	Co	Ni	
A700	κ	$a = 5.0599$ $c = 18.5037$	27.26 ± 1.38	33.46 ± 0.68	39.28 ± 1.26	74
	σ	$a = 4.6226$ $c = 8.9189$	50.86 ± 1.74	29.84 ± 1.23	19.30 ± 0.86	26
A800	κ	$a = 5.0631$ $c = 18.5304$	28.31 ± 0.69	33.47 ± 0.39	38.22 ± 0.51	75
	σ	$a = 4.6129$ $c = 8.8992$	48.55 ± 0.47	30.69 ± 0.41	20.76 ± 0.10	25
A900	FCC	$a = 3.6015$	32.44 ± 0.19	32.86 ± 0.39	34.70 ± 0.39	95
	κ	$a = 5.0742$ $c = 18.6109$	28.88 ± 0.20	36.38 ± 0.27	34.74 ± 0.32	5
A1000	FCC	$a = 3.6006$	32.18 ± 0.31	33.84 ± 0.29	33.98 ± 0.37	100
A1200	FCC	$a = 3.6003$	32.83 ± 0.85	32.94 ± 0.81	34.23 ± 0.49	100

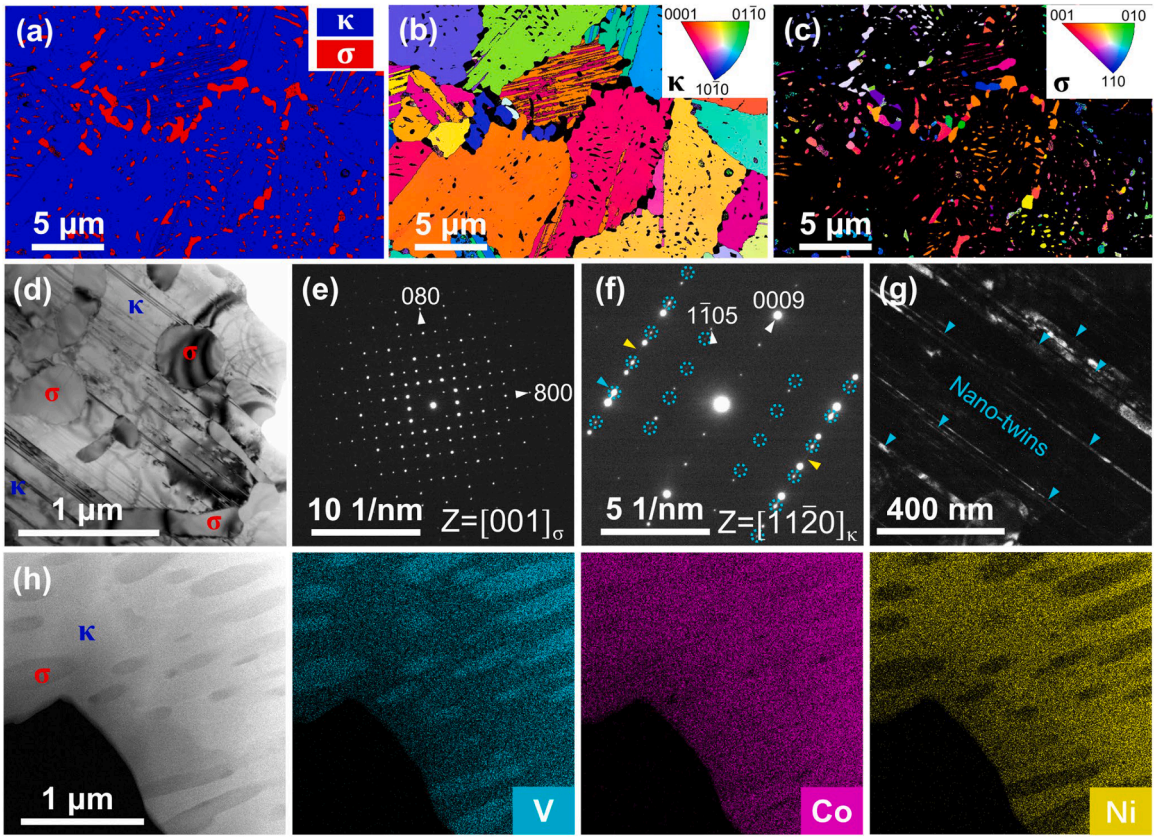

Fig. 2. Multiscale microstructural characterizations of the A800 alloy. (a) EBSD phase map showing the distributions and morphologies of the κ and σ phases, and inverse pole figure along the Z direction (IPF-Z) maps of the (b) κ phase and (c) σ phase. (d) TEM BF image showing the detailed appearances of the σ and κ phases with the corresponding SAED patterns of the (e) σ and (f) κ phases, respectively. Some diffraction spots of these two phases are representatively indexed and pointed in (e) and (f) by white arrows. Moreover, the streaks in (f) (pointed by yellow arrows) are illustrative of the SFs along the (0001) basal plane. (g) TEM DF image corresponding to the diffraction spot pointed by the cyan arrow in (f), revealing the existence of nano-spaced annealing nano-twins in the κ phase. (h) HAADF-STEM image and the corresponding EDS maps of V, Co, and Ni.

and corresponding EDS maps (Fig. 2**(h)**). Overall, V is enriched in the σ phase, while Co and Ni partition to the κ phase. The chemical compositions of the κ and σ phases in the A800 sample are listed in Table 1. It can be noticed that the V contents of the κ phases ($V_{28.31}Co_{33.47}Ni_{38.22}$) are slightly higher than that of the previously reported $V_{25}Co_{37.5}Ni_{37.5}$ phase [73], which suggests that the atomic occupation of the present κ phase might be different from that of the ideal model — $V(Co, Ni)_3$. Similarly, the composition of the σ phase ($V_{48.55}Co_{30.69}Ni_{20.76}$; $V_x(Co, Ni)_y$, $x : y \approx 1 : 1$) also deviates from that of previously reported $V_{62}Co_{38}$ phase ($x : y \approx 3 : 2$) [72]. Such noticeable inconsistencies will be discussed in the later atomic-scale analyses of the κ and σ phases (see Section 4.2). Furthermore, based on the EDS results, the volume fractions of the κ and σ phases in the A800 alloy can be determined using the lever rule [74,75] (**Fig. S3**) as 75 % and 25 %, respectively, as summarized in Table 1.

As pointed out in the Introduction, three different structures were reported in the alloy annealed at 900 °C for various time, *i.e.*, FCC [52], FCC + $L1_2$ [24], and FCC + κ [58]. In this work, only a single FCC phase could be identified in the A900 sample from the XRD profile (Fig. 1); however, the following EBSD and TEM characterizations reveal that the thermostabilized state at 900 °C is a dual-phase structure (Fig. 3). The EBSD phase map (Fig. 3**(a)**) shows that the A900 alloy consists of the equiaxed FCC grains (with a mean size of ~ 64 μm) and the lath-shaped κ precipitates at grain boundaries (with a mean size of ~ 3 μm). Additionally, annealing twins are commonly discovered in the κ phase and FCC matrix, as shown in the EBSD IPF-Z map (Fig. 3**(b)**). To obtain more crystallographic information, the flat interface between two phases in the TEM BF image (Fig. 3**(c)**) is especially of interest. The interphase SAED pattern (Fig. 3**(d)**) suggests that the preferred $(0001)_\kappa/(111)_{FCC}$ interface should be flat, and the FCC and κ phases have orientation relationships of $[11\bar{2}0]_\kappa/[110]_{FCC}$ and $(0001)_\kappa/(111)_{FCC}$. Moreover, the atomic-scale HAADF-STEM images along the $[11\bar{2}0]_\kappa/[110]_{FCC}$ (Fig. 3**(e)**) and $[10\bar{1}0]_\kappa/[121]_{FCC}$ directions (Fig. 3**(f)**) unveil that the $(0001)_\kappa/(111)_{FCC}$ interface is not only atomically flat but also nearly fully coherent with a subtle lattice misfit of 0.38 % (calculated using the lattice parameters in Table 1 [76]).

The 3D-APT analysis was performed to further investigate the chemical partitioning of all elements, as shown in **Fig. 3(g)** and Fig. 3**(h)**. The elemental maps present that the distribution of constituent elements within the studied volume is seemingly homogenous (Fig. 3**(g)**). However, the proxigram reveals that Co tends to weakly partition to the κ phase, and V slightly depletes in it, as shown in Fig. 3**(h)**. Table 1 then summarizes the compositions of the FCC phase ($V_{32.44}Co_{32.86}Ni_{34.70}$ (at. %)) and κ phase ($V_{28.88}Co_{36.38}Ni_{34.74}$ (at.%)). Such a tiny compositional difference between the FCC matrix and the κ precipitate would make the lever-rule-based calculation inexecutable, so the volume fractions were referred to the values given by the EBSD phase map (Fig. 3**(a)**) instead, *i.e.*, 95 % for the FCC phase and 5 % for the κ phase, as listed in Table. 1. Therefore, it is reasonably inferred that the amount of the κ precipitates is too little to be detected by XRD (Fig. 1).

The EBSD phase maps of the A1000 (**Fig. S4(a)**) and A1200 (**Fig. S4 (c)**) alloys disclose the single FCC structures, consistent with the XRD result (Fig. 1). Also, the microstructures of both alloys are comprised of the equiaxed and fully recrystallized grains with the average grain sizes of ~ 66 μm for the A1000 alloy and ~ 122 μm for the A1200 alloy, as shown in the EBSD IPF-Z maps (**Fig. S4(b)** and **Fig. S4(d)**).

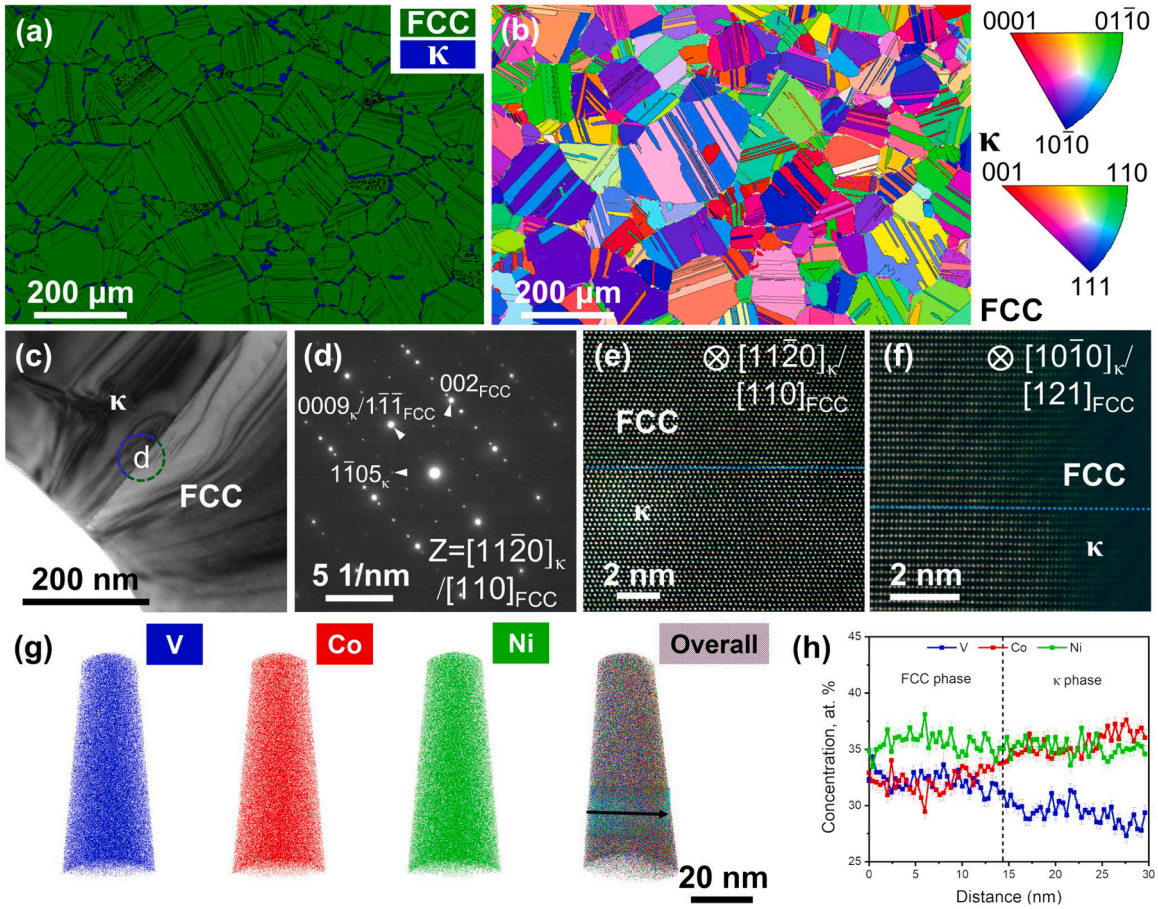

Fig. 3. Multiscale microstructural characterizations of the A900 alloy. (a) EBSD phase map and (b) IPF-Z map showing the distributions and morphologies of the FCC and κ phases. (c) TEM BF image displaying the interface between the FCC and κ phases. (d) SAED pattern taken from the region 'd' in (c), revealing an orientation relationship of $<11\bar{2}0>_κ/<110>_{FCC}$ and $\{0001\}_κ/\{111\}_{FCC}$. HAADF-STEM images along (e) $[11\bar{2}0]_κ/[110]_{FCC}$ direction and (f) $[10\bar{1}0]_κ/[121]_{FCC}$ direction, exhibiting the atomic-scale microstructure of the interface. (g) V, Co, and Ni atom maps in a typical APT tip lifted out from the interphase region, unveiling the subtle compositional difference. (h) Proxigram of concentration profiles (bin width = 0.4 nm) extracted from the region marked by the cyan cylinder in (g) (diameter = 20 nm), displaying the chemical partitioning in the FCC and κ phases.

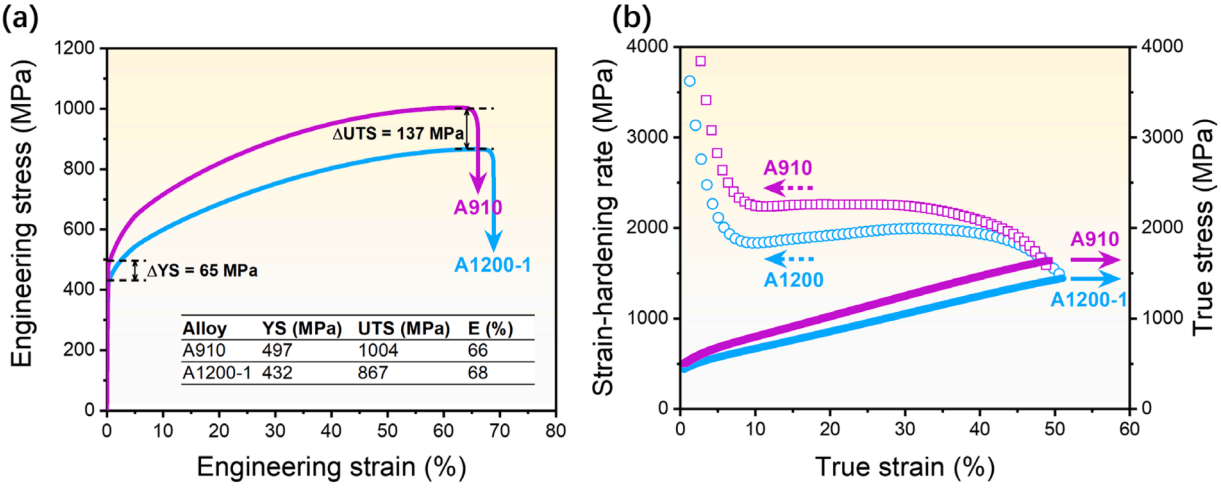

Fig. 4. Tensile properties and fracture surfaces of the A700, A900, and A1200 alloys. (a) Engineering stress-strain curves of the A900 and A1200 alloys, including values of yield stress (YS), ultimate tensile stress (UTS), and elongation (E) summarized in the inset table. (b) True stress-strain curves and the corresponding strain-hardening rates of the A900 and A1200 alloys.

3.3. Mechanical properties of the VCoNi MEAs after long-term annealing treatments

Uniaxial tensile tests were performed at room temperature to study the deformation behaviors of each specimen after long-term annealing. It should be noted that all the A700 and A800 tensile specimens fractured before yielding due to the extremely brittle nature of the κ + σ structure (**Fig. S5**), so they are excluded in the following analysis. Fig. 4 **(a)** displays the engineering stress-strain curves of the A900 and A1200 alloys. Specifically, both alloys have comparable ductility (64 % for the A900 alloy; 65 % for the A1200 alloy). With the increase in the annealing temperature, yield strength decreases from 514 MPa for the A900 alloy to 391 MPa for the A1200 alloy; meanwhile, ultimate tensile strength decreases from 1032 MPa for the A900 alloy to 792 MPa for the A1200 alloy. Furthermore, the corresponding true stress-strain curves and strain-hardening rates are presented in Fig. 4**(b)**. It can be seen that the strain-hardening rate of the A900 alloy is evidently higher than that of the A1200 alloy. Also, within the true strain ranging from 10 % to 30 %, the A1200 alloy exhibits an upward trend in the strain-hardening rate, while the A900 alloy keeps a constant trend. Different values and trends of strain-hardening rates may suggest varied deformation mechanisms; however, since the grain sizes and phase structures of both alloys are distinct, detailed comparisons of the strengthening mechanisms could be less informative. Additional tensile testing with special consideration of grain size and phase structure will be conducted to evaluate the potential SRO strengthening (see Section 4.3).

The deformation microstructure of the tensile fractured A900 specimen was inspected using EBSD and TEM, as shown in **Figs. S6** and Fig. 5, respectively. The TEM two-beam BF characterization on an FCC grain (Fig. 5**(a)**) confirms that extensive planar slip dislocations and dislocation tangles are activated, as marked by the cyan dashed lines and magenta dashed circles, respectively, in Fig. 5**(a)**. The accumulation of dislocations near the interface between the two phases was also observed, as shown in Fig. 5**(b)**, which suggests that dislocations had difficulty in penetrating the phase boundary. Moreover, we observed high-density dislocations inside the κ phase, as shown in Fig. 5**(b)–(d)**. To determine the Burgers vector of dislocations gliding in the κ phase, the g/3 g WBDF conditions with c-extinction (Fig. 5**(c)**) and a-extinction (Fig. 5**(d)**) were adopted to image dislocations at the same place. Some dislocations could only be detected under the c-extinction condition, which suggests that these dislocations are the ⟨a⟩ dislocations. Additionally, visible dislocations in Fig. 5**(d)** mean that dislocations possessing the ⟨c⟩ components can be activated to slip in the κ phase, which is significantly different from the dislocation configurations of a previously investigated $Ni_3(Ti_{0.90}Nb_{0.10})$-type κ phase (where ⟨a⟩ dislocations were dominant) [77,78]. All in all, our findings suggest that the deformation microstructure of the FCC in the A900 specimen was not dominated by either planar slip [52] or wavy slip [24], but both deformation characteristics (the coexistence of profuse dislocation arrays and dislocation tangles in Fig. 5**(a)**). In addition, none of the obvious SF, DT, and phase transformation were unveiled.

To unravel the atomic-scale deformation mechanisms, dislocations in the FCC and κ phases of the fractured A900 specimen were further characterized using the atomic-resolution HAADF-STEM, as shown in Fig. 5**(e)–(h)**. Substantially, most edge dislocations observed in the FCC matrix are full dislocations with the Burgers vector of $\frac{a_{FCC}}{2}[101]$, as shown in Fig. 5**(e)**, which have compact cores (**Figs. S7(a)–(b)**) rather than split into two partial dislocations, indicating a high SFE of the A900 alloy. Additionally, we found the Lomer lock in the FCC phase, as shown in Fig. 5**(f)**. Extra half-planes of $(\bar{1}\bar{1}1)$ and (111) can be identified, which is consistent with the corresponding ε_{xx} (**Fig. S7(c)**) and ε_{yy} (**Fig. S7(d)**) strain maps. In this case, the Lomer lock with the Burgers vector of $\frac{a_{FCC}}{2}[110]$ was formed by the reaction of two full dislocations with Burgers vectors of $\frac{a_{FCC}}{2}[011]$ and $\frac{a_{FCC}}{2}[10\bar{1}]$ on the $(\bar{1}\bar{1}1)$ and the (111) planes, respectively:

$$\frac{a_{FCC}}{2}[011]+\frac{a_{FCC}}{2}[10\bar{1}]\rightarrow\frac{a_{FCC}}{2}[110] \quad (3)$$

The derived Burgers vector is parallel to neither of the slip planes of the reactant dislocations, resulting in a sessile dislocation junction. Therefore, the Lomer locks can impede the slip of mobile dislocations and act as the Frank-Read sources for dislocation multiplication, which was reported to be responsible for improving the strain-hardening rate [79].

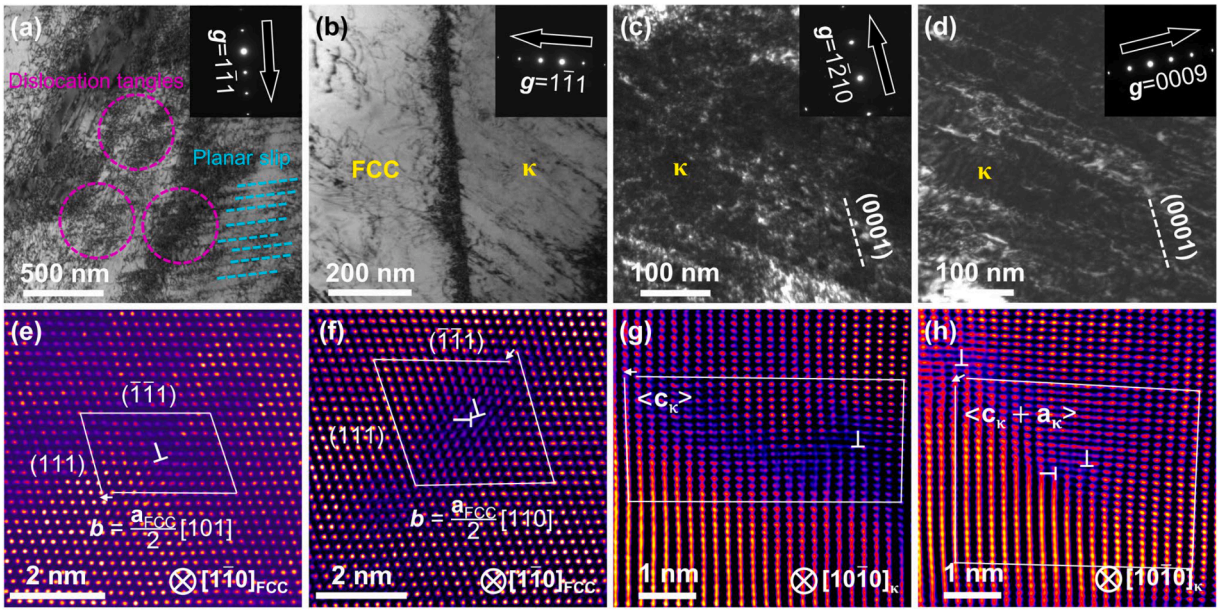

Fig. 5. Dislocation structures in the fractured A900 specimens. TEM two-beam BF images of (a) FCC matrix and (b) interface between the FCC and κ phases, taken nearly along the [110] direction with a reflection vector of $g = [1\bar{1}1]$. TEM WBDF images of the κ phase taken at the same place, nearly along the $[\bar{1}0\bar{1}0]$ direction with reflection vectors of (c) $g = [12\bar{1}0]$ and (d) $g = [0009]$. Atomic-resolution HAADF-STEM images of (e) nearly perfect edge dislocation and (f) Lomer lock in the FCC phase; (g) ⟨c⟩ and (h) ⟨c + a⟩ dislocations in the κ phases. Burgers circuits and Burgers vectors (*b*) are delineated by the white solid lines and arrows, respectively, and the extra half-planes of atoms are denoted by the 'T' symbols. The corresponding GPA ε_{xx} and ε_{yy} strain maps are shown in **Fig. S7**.

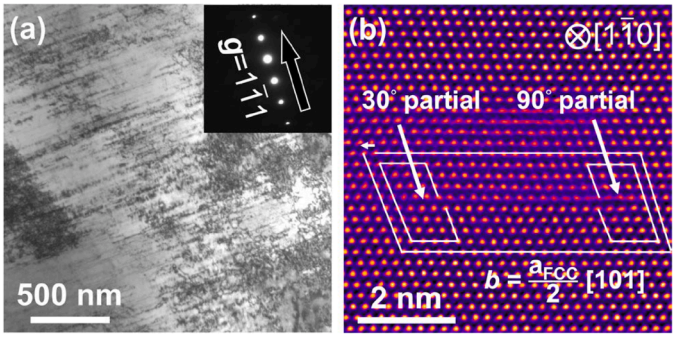

Fig. 6. Dislocation structures in the fractured A1200 specimens. (a) TEM two-beam BF image taken nearly along the [110] direction with a reflection vector of $g = [1\bar{1}1]$, showing the dislocation substructure in an FCC grain. (b) HAADF-STEM image of a typical SF between Shockley partials (a dissociated 60° dislocation).

Apart from the dislocations in the FCC matrix, the atomic structures of the dislocations in the κ phase were carefully investigated using HAADF-STEM along the $[\bar{1}0\bar{1}0]$ direction. Not only ⟨c⟩ dislocations (Fig. 5**(g)**) but also ⟨c + a⟩ (Fig. 5**(h)**) dislocations can be clearly revealed. The dilatation-contraction pairs shown in **Fig. S7(g)** and **Fig. S7(h)** manifest the ⟨c⟩ and ⟨a⟩ components of the mixed dislocation (Fig. 5**(h)**), respectively. Combined with the evidence of high-density dislocations with the ⟨c⟩ component (Fig. 5**(d)**), there should be numerous ⟨c + a⟩ dislocations activated in the κ phase during the plastic deformation, guaranteeing the surprising deformability of the κ phase.

In the same way, the deformation microstructure of the tensile fractured A1200 specimen was inspected using EBSD and TEM, as shown in **Fig. S6** and Fig. 6, respectively. Neither potential DT nor phase transformation could be observed. Detailed dislocation configurations are disclosed in the TEM two-beam BF image (Fig. 6**(a)**). It can be seen that planar-typed dislocation substructures, including slip traces and high-density dislocation walls, were widely activated, together with few wavy dislocations. Furthermore, compared to dislocations with narrow cores in the A900 specimen, partial dislocations with a wider separation distance (~ 4 nm) were unveiled, as shown in the atomic-resolution HAADF-STEM image (Fig. 6**(b)**), implying a lower SFE of the A1200 alloy. It should be noted that the chemical compositions of the FCC phases in both specimens (listed in Table 1) are so close that SFE should not vary markedly to affect the dissociation distance. Hence, SRO developed at 900 °C [24] can be most likely regarded as a critical factor responsible for the change in SFE, which will be quantitatively discussed in Section 4.3.

4. Discussion

4.1. Thermodynamic instability of the VCoNi alloy

Preliminary results demonstrated that the VCoNi alloys can achieve various yet remarkable properties by tailoring their phase structures [52–55], serving as rising structural materials in many fields. For example, the σ + κ structured VCoNi alloy exhibits super plasticity at high strain rates [54], while the FCC structured has a superior combination of strength and ductility at room temperature, accompanied by high resistance to hydrogen embrittlement [52,53,55]. Therefore, the performances of the VCoNi alloys depend crucially on the heat treatments guided by the theoretically calculated phase diagrams. However, as mentioned above, the previous CALPHAD results of the VCoNi alloy using different databases were not entirely consistent with the experimental results [53–55]. The calculated phase diagram using the TCHEA3 database [53], for example, showed that the σ and FCC phases presented within 700–800 °C without the κ phase, and the single-phase FCC structure appeared above ~ 750 °C. With reference to another using the TCFE5 database [54,55], the eutectoid transformation (σ + κ → FCC) started at 757 °C, the dual-phase structure (FCC + κ) was kept within 700–800 °C, and the single-phase FCC structure was expected to be obtained above 800 °C. Apparently, according to the microstructures of the A800 (Fig. 2**)**, A900 (Fig. 3), and A1000 (**Fig. S4**) alloys, critical temperatures of two types of phase transformations, *i.e.*, σ + κ → FCC and FCC + κ → FCC, as well as the single FCC phase region, were significantly underestimated by these theoretical calculations.

To precisely determine the critical phase transformation temperatures, we further performed isothermal long-term heat treatments at 850, 860, 870, and 910 °C, respectively, along with EBSD phase mapping of these alloys, as shown in **Fig. S8**. The eutectoid transformation (σ + κ → FCC) happens in a narrow temperature range (< 20 °C) with a starting temperature of 850–860 °C and an ending temperature of 860–870 °C. Considering the presence of the κ phase in the A900 specimen (Fig. 3), the FCC + κ two-phase region should be only ~ 30 °C, ranging from 860–870 °C to 900–910 °C. Lastly, the lower boundary of the single-phase region should be located at 900–910 °C. Taking all microstructural results (Table 1 and **Fig. S8**) into account, here we propose a schematic phase diagram plotting the volume fractions of all phases as functions of temperature, as shown in Fig. 7. In view of this, to achieve desired phase structures, heat treatment temperature should be precisely controlled.

4.2. Atomistic understanding of the σ and κ phases

Two constituent intermetallic phases, κ and σ, have been identified in Section 3.2, with ICSD-compositions of $Co_{37.5}Ni_{37.5}V_{25}$ and $V_{62}Co_{38}$ (at. %), respectively. However, the measured V contents of the κ and σ phases (Table 1) are somehow higher (~ 3 at.%) and lower (~ 13 at.%), respectively, than that provided by the ICSD database. Therefore, we further shed atomic-scale light on the crystal structures of the κ and σ phases for a better understanding.

Figure 8(a) shows the experimental SAED pattern along the [0001] zone axis of the κ phase in the A800 alloy. Interestingly, in some areas, the extra super-diffraction spots (circled in cyan) were discovered in addition to the regular diffraction spots of the κ phase (circled in half-yellow/half-cyan). Previous investigations ascribed the observed 1/3 {422} forbidden reflections in the [111] SAED patterns of Ag and Si to the planar defects such as SFs and twins [46–48], so, to figure out whether these extra super-diffraction spots in Fig. 8**(a)** appear in the same way, we simulated the diffraction patterns along the same

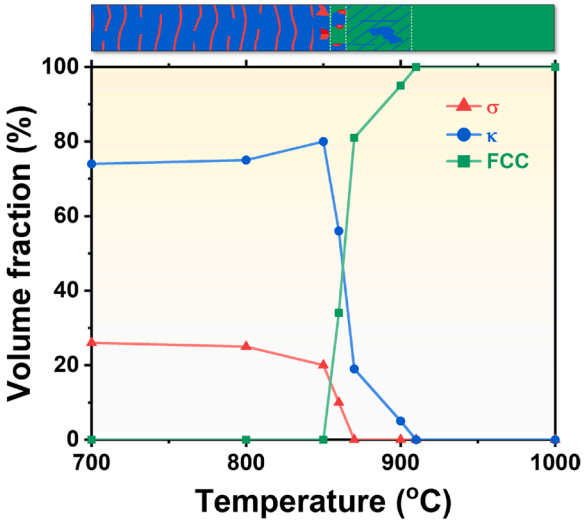

Fig. 7. Schematic illustration of the volume fractions of all phases in the VCoNi alloy as functions of temperature. The data points are sourced from Table 1 and **Fig. S8**.

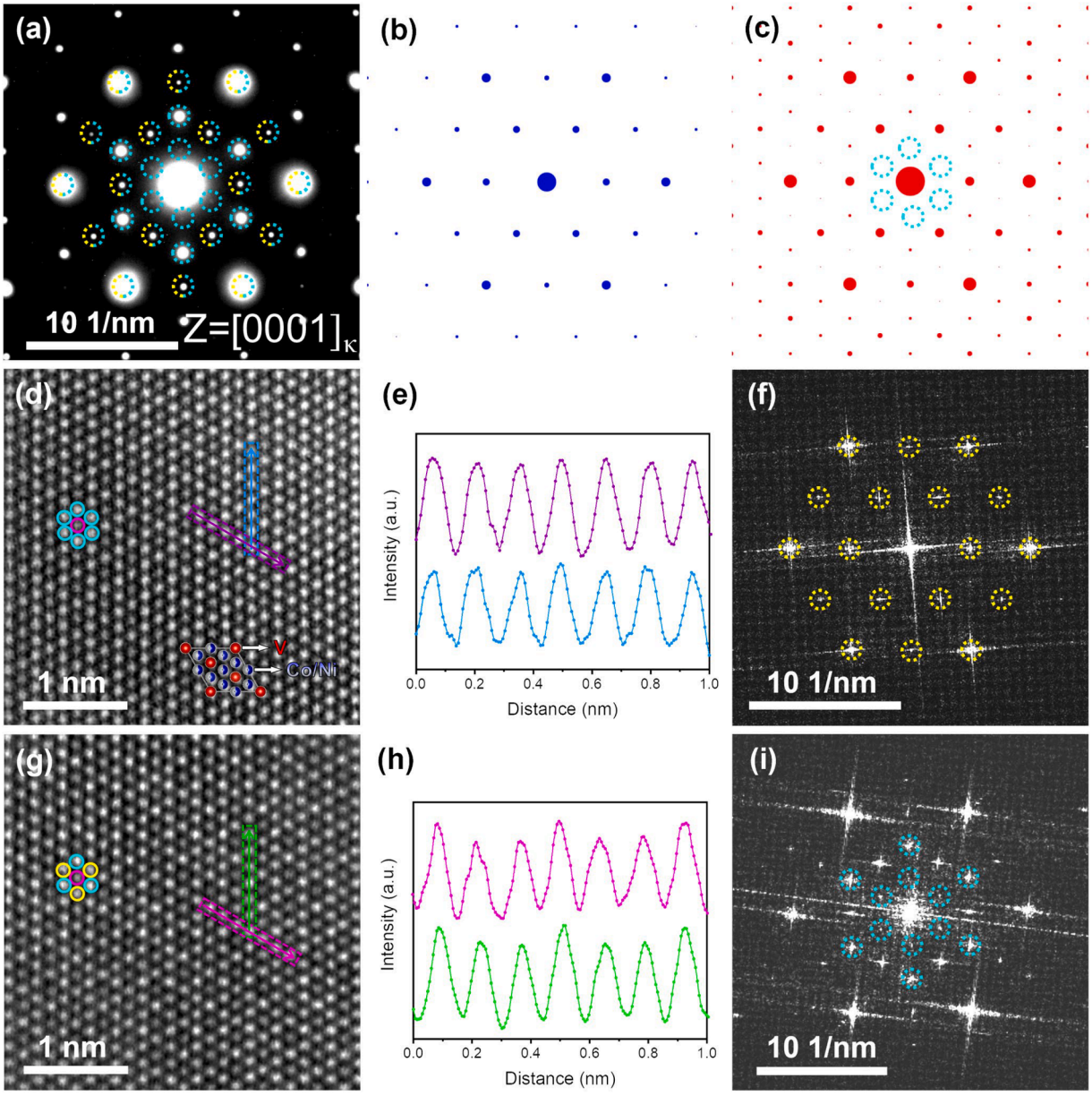

Fig. 8. The atomic structure of the κ phase and κ′ phase in the A800 alloy. (a) Experimental SAED pattern along the [0001] zone axis of the κ phase. The simulated SAED patterns along the [0001] zone axis of the κ phase (b) with and (c) without the twin structure (**Fig. S9**). (d) and (g) HAADF-STEM images of the κ and κ′ phases, respectively. (e) and (h) Intensity profiles of the corresponding arrows in (d) and (g), respectively. (f) and (i) FFT images corresponding to (d) and (g), respectively. The superimposed inset in (b) is the corresponding unit cells.

direction of the κ phase without and with twin boundaries (**Fig. S9**), as shown in Fig. 8**(b)** and Fig. 8**(c)**, respectively. Most observed diffractions in Fig. 8**(a)** can be well-fitted by the twin-considered simulation (Fig. 8**(c)**) except for six satellite spots around the central beam, whose corresponding locations are also circled in cyan in Fig. 8**(c)**. That is, the presence of the extra super-diffraction spots could not be solely attributed to the existence of planar defects, and what is more, an additional chemical order, presumably referred to as κ′ phase, in real space should be considered.

Atomic-resolution HAADF-STEM images of the κ (Fig. 8**(d)–(f)**) and κ′ (Fig. 8**(g)–(i)**) phases in the A800 alloy were examined for comparing the periodic intensity of atom columns. It is known that the contrast of the HAADF-STEM image is proportional to Z^n, where Z is the atomic number, and n is between 1.6 and 1.9, depending on the inner and outer solid angles of the ADF detector [80]. As for this work, the atomic intensities of Co ($Z = 27$) and Ni ($Z = 28$) should be very close and higher than that of V ($Z = 23$). By applying this principle to the HAADF-STEM image of the κ phase (Fig. 8**(d)**), the darker V atom column (circled in magenta) is surrounded by six random Co/Ni atoms (circled in cyan) with a similar higher contrast (Fig. 8**(e)**). The corresponding FFT pattern of Fig. 8**(f)** is consistent with the simulated SAED pattern of the typical κ phase (Fig. 8**(b)**). On the other hand, the HAADF-STEM image of the κ′ phase (Fig. 8**(g)**) not only reveals the intensity difference between the central atom columns (circled in magenta) and surrounded six atom columns (circled in cyan and yellow), but also unveils the periodic intensity difference among the surrounded atom columns—the intensity of the cyan-circled atom columns is higher than that of the yellow-circled (Fig. 8**(h)**). This additional periodic intensity difference as well as the additional spots (circled in cyan) in the corresponding FFT pattern (Fig. 8**(i)**) strongly support the existence of the κ′ phase. Specifically, the yellow-circled atom columns, which should be the random Co/Ni atom columns in the typical κ phase, are partially replaced by V atoms.

Moreover, no sharp κ/κ′ interface could be observed, as shown in **Fig. S10**, indicating that these two phases are fully coherent and formed via spinodal decomposition [81,82]. As a result, the existence of the κ′ phase can reasonably explain why the contents of V in the κ phase measured by TEM-EDS and APT (Table 1) are higher than the standard value provided by the ICSD database (25 at.%).

Concerning the measured chemical composition of the σ phase that significantly deviates from the stoichiometry adopted by the previous research on the VCoNi alloy [54], we suggest that other databases should be considered instead of the $V_{62}Co_{38}$ by simulating the experimental observations [72]. It is noted that the compositional disorder of the σ phase is unusually large and widely reported in addition to the ideally ordered stoichiometry of A_2B [83]. After several non-stoichiometric systems were reviewed, the $Cr_{49.5}Fe_{50.5}$-type σ phase (ICSD: 102,747) [84] was selected for the following structural simulations due to its similar lattice constants (a = 4.558; c = 8.797 Å) and compositional ratio ($A : B \approx 1 : 1$) (Table 1). Then, we further contemplated the feasibility of examinations using electron diffraction and XRD. Even though the simulated SAED (**Fig. S11(a)–(b)**) and XRD (**Fig. S11(c)**) patterns of $V_{62}Co_{38}$ and $Cr_{49.5}Fe_{50.5}$ show different intensities at similar peak positions, the relative intensities could be experimentally influenced by the sample thickness (for SAED) and texture (for XRD), which is unfavorable for differentiating subtle crystal structures. Alternatively, we carefully characterized the atomic structure of the σ phase in the A800 alloy by using the atomic-scale HAADF-STEM along different low-index zone axes and then compared them with simulation results along the exact directions using $V_{62}Co_{38}$ and $Cr_{49.5}Fe_{50.5}$ databases, as shown in Fig. 9. When the zone axis [001] is chosen, the distorted pentagonal building blocks (outlined in cyan) can be revealed in the experimental HAADF-STEM (Fig. 9**(a)**) and $Cr_{49.5}Fe_{50.5}$-simulated (Fig. 9**(c)**) images, but absent in the $V_{62}Co_{38}$-simulated image (Fig. 9**(b)**). In contrast, the HAADF-STEM image (Fig. 9**(d)**) viewed from the other zone axis — [110] looks as if it is composed of rectangular building blocks, the same as the simulated results using both databases (Fig. 9**(e)** and Fig. 9**(f)**). However, with more details, two atom columns at the center of the rectangular building block are surrounded by six brighter atom columns in the experimental (Fig. 9**(d)**) and $Cr_{49.5}Fe_{50.5}$-simulated (Fig. 9**(f)**) images but by four in the $V_{62}Co_{38}$-simulated image (Fig. 9**(e)**). As a result, the crystal structure of the σ phase precipitating in the VCoNi alloy can be eventually identified as the $Cr_{49.5}Fe_{50.5}$-type structure rather than the $V_{62}Co_{38}$-type, agreed by the measured chemical compositions (Table 1).

4.3. *Effects of SRO on SFE and deformation mechanisms*

Given that the FCC phases of the A900 and A1200 alloys had similar chemical compositions (Table 1) but opposite tendencies toward dislocation dissociation, as shown in Fig. 5**(a)** and Fig. 6**(a)**, respectively, we further quantitatively measured the SF widths at the atomic scale and estimated corresponding SFEs. It should be noted that SFs are rarely seen in both alloys, and their widths are extremely narrow, suggesting the high SFEs of them that cannot be explained by previous DFT results [56]. After tens of dislocations were examined, Fig. 10**(a)–(c)** and Fig. 10**(d)–(f)** representatively present the atomic structures of the observed SFs in the A900 and A1200 alloys, respectively. More instances of SFs are displayed in **Fig. S12**. The separation distances of partials can range from 1.25 nm to 0.54 nm for the A900 alloy and from 10.39 nm to 1.24 nm for the A1200 alloy. In general, SFs in the A900 alloy were imperceptible due to the compact nature of dislocation cores (Fig. 10**(a)–(c)** and **Fig. S12(a)–(c)**). On the contrary, dislocations in the A1200 alloy inclined to dissociate into partials with wider separation distances, even for screw dislocations (**Fig. S12(d)–(e)**). As SFs were absent in the

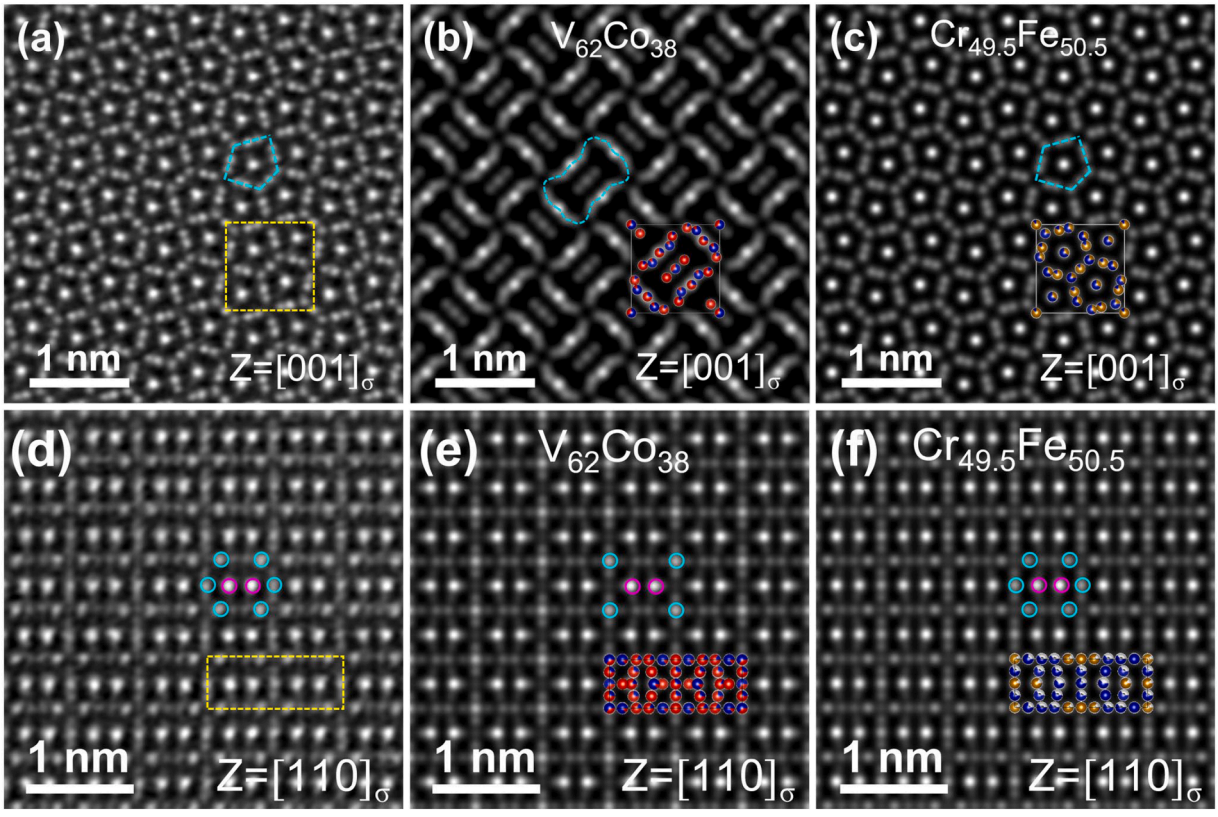

Fig. 9. Comparisons between the experimental atomic-resolution HAADF-STEM images of the σ phase in the A800 alloy and simulated images of the $V_{62}Co_{38}$ phase and $Cr_{49.5}Fe_{50.5}$ phase. (a) Experimental HAADF-STEM images of the σ phase as well as the simulated HAADF-STEM images of the (b) $V_{62}Co_{38}$ and (c) $Cr_{49.5}Fe_{50.5}$ phases along the [001] direction. The building blocks are outlined in cyan. (d) Experimental HAADF-STEM images of the σ phase as well as the simulated HAADF-STEM images of the (b) $V_{62}Co_{38}$ and (c) $Cr_{49.5}Fe_{50.5}$ phases along the [110] direction. The superimposed insets in (b), (c), (e), and (f) are the corresponding unit cells.

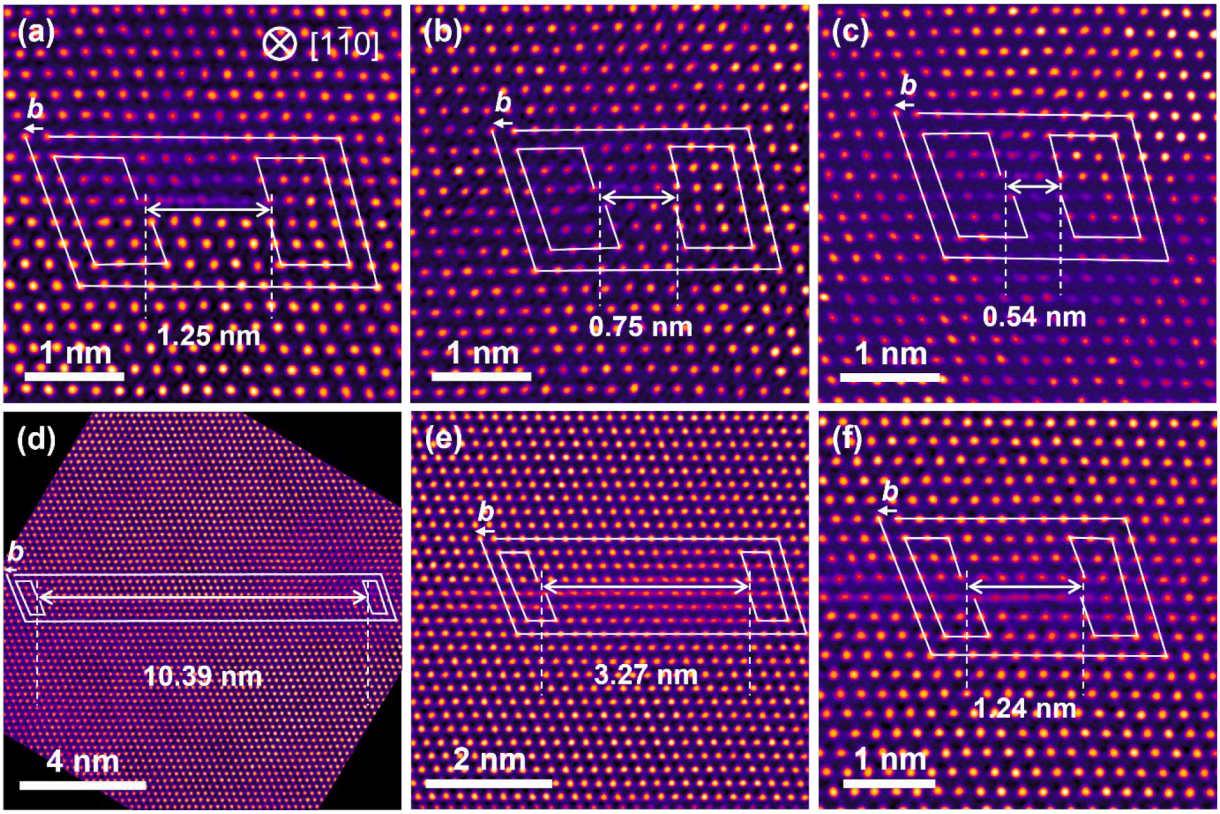

Fig. 10. Atomic-resolution HAADF-STEM images showing dissociations of 60° dislocations into Shockley partials with various SF widths in the (a)–(c) A900 and (d)–(f) A1200 alloys. More instances are presented in **Fig. S12**.

previous research on the VCoNi alloy, we consider that the separation distances were beyond the resolution limits of the chosen techniques, such as contrast images in SEM or TEM [52,53,55–57]. Here, by using the atomic-resolution HAADF-STEM, the SF-mediated deformation was proven to be activated in the VCoNi alloy, which should not be ignored when the deformation mechanism was discussed.

In addition to the noticeable increasing/decreasing tendency of dislocation dissociation, significant variations in SF widths were revealed, especially in the A1200 alloy. The largest observed separation distance (10.39 nm in Fig. 10**(d)**) is over 8 times wider than the narrowest one (1.24 nm in Fig. 10**(f)**). A similar range of variation (± 3.4 nm) was also found in the equiatomic CrCoNiFeMn HEA with a mean separation distance of 4.82 nm. It should be noted that for typical FCC metals, the average range in separation distances is only about ± 0.45 nm [49], which is undoubtedly far less than that of our observations in the A1200 alloy (Fig. 10**(d)–(f)**) but still reasonable for that in the A900 alloy (Fig. 10**(a)–(c)**). To interpret such difference in the amplitude of variations between the A900 and A1200 alloys, the separation distance was viewed from the perspective of SFE (Fig. 11**(a)**):

$$\mathrm{SFE} = \frac{\mu b_p^2}{8\pi d}\frac{2-\nu}{1-\nu}\left(1-\frac{2\nu\cos 2\theta}{2-\nu}\right) \quad (4)$$

where μ is the shear modulus ($\mu = 78$ GPa), b_p is the Burgers vector of 1/6 < 112> partial dislocations ($b_p = 0.147$ nm), ν is the Poisson's ratio ($\nu = 0.318$), θ is the dislocation character angle ($\theta = 60°$), and d is the dislocation dissociation distance between two partials. The A900 and A1200 exhibit approximately identical values of μ and ν, measured by using the ultrasonic pulse-echo technique, as listed in **Table S2**. By substituting observed values of d (Fig. 10 and **Fig. S12**) into Eq. (4), Fig. 11**(a)** demonstrates that despite the relatively small variation in dissociation distance, the estimated SFE of the A900 alloy could vary from 157 to 364 mJ/m^2 with a distribution width of 207 mJ/m^2, while that of the 1200 alloy has a comparable wide distribution (140 mJ/m^2) ranging from 19 to 159 mJ/m^2. That is, compared to the A1200 alloy, the A900 alloy possesses not only a higher SFE but also an even wider range of variations in the 'local SFE'. This abnormal increase in the global SFE at a particular annealing temperature and locally fluctuated SFE may explain why DT was absent in the VCoNi alloy even though the calculated SFE (~ 30 mJ/m^2 [56]) was still within the reported range of triggering DT (20–40 mJ/m^2 [85]), as remarked in Fig. 11**(a)**. Additionally, the higher SFE of the A900 alloy is in concurrence with the observed mixed dislocation configuration (Fig. 5**(a)**), while the planar slip is more pronounced in the A1200 alloy due to the lower SFE (Fig. 6**(a)**).

After the dislocation structures and deformation mechanisms were understood from the viewpoint of SFE, we further clarified the origin of the influence on SFE through the computation approach. Since the chemical compositions of the FCC phases in the A900 and A1200 alloys were nearly identical, and none of the nanoscale precipitates could be found in the FCC phases of both alloys, here, SRO is reasonably regarded as the key to controlling the SFE. Recently, Zhu and Wu adopted the DFT-MC simulations to compare the effects of SROs on the SFEs of three prototype FCC MEPAs, *i.e.*, equiatomic CrCoNiFeMn, CrCoNi, and VCoNi alloys [50]. In the SQS state, the VCoNi alloy was predicted to have the highest mean SFE (19 mJ/m^2) with the largest standard deviation (± 98 mJ/m^2) among three alloys, as well as significant variations in the local SFE (ranging from−151 to 198 mJ/m^2) in different {111} slip planes, resulting from by non-negligible solute fluctuations. In contrast, in the SRO state optimized by the MC simulation at 227 °C (500 K), three alloys showed significant increasing tendencies in the mean SFEs, among which the VCoNi alloy experienced the largest increment in SFE and still exhibited the highest mean SFE (226 mJ/m^2) with similarly considerable standard deviation (± 81 mJ/m^2) as well as local fluctuations (ranging from 82 to 350 mJ/m^2) on different {111} slip planes. To our surprise, this foresighted calculation and our observations (the

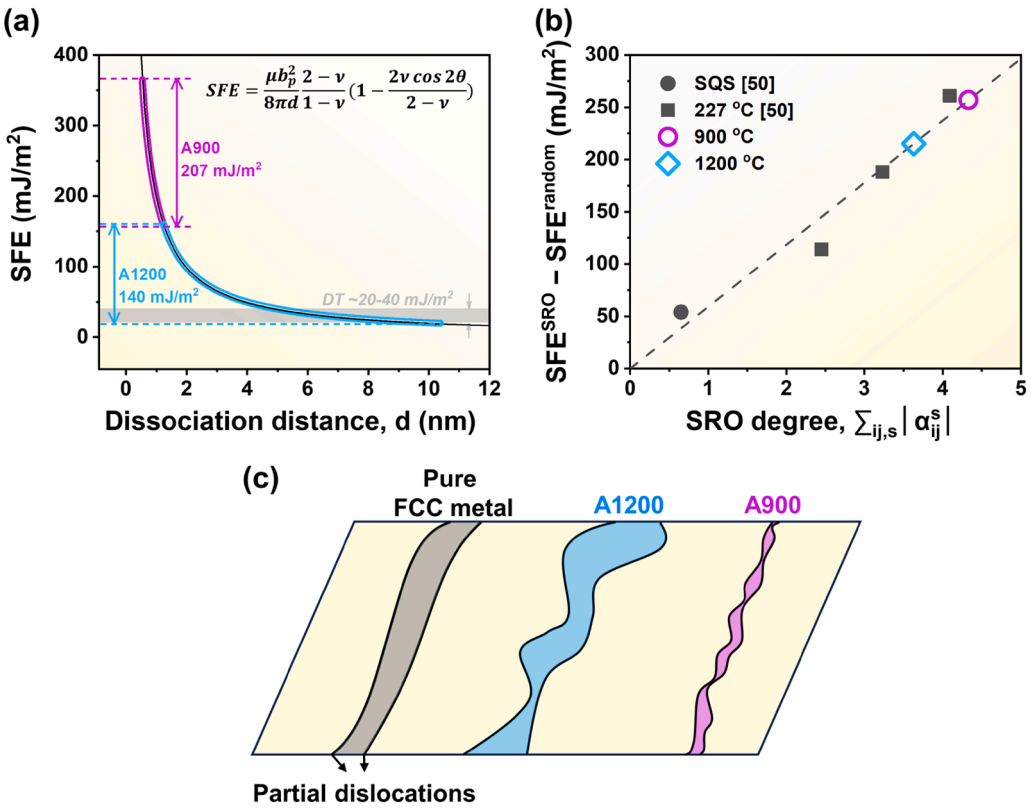

Fig. 11. Influences of SRO on SFE and deformation mechanisms. (a) SFE platted as a function of dissociation distance between partial dislocations, with experimentally observed SFE ranges of the A900 and A1200 alloys. (b) Linear relationship between the change in SFE (SRO state relative to random state) and the SRO degree. The slope was fitted by the data points from *ref.* 50; the magenta circle and cyan diamond represent the MC-simulated SRO degrees at 900 °C and 1200 °C — 4.33 and 3.63, respectively. (**Fig. S1**). (c) Schematic illustration of dislocation dissociation into two partials in the pure FCC metal, A1200, and A900 alloys.

SRO-induced increasing SFE and a wide variation in local SFE) can complement each other. However, the FCC structure was ideally assumed in their DFT-MC simulations performed at 227 °C, which is evidently in the eutectoid zone (σ + κ structure below ~ 860 °C) of the VCoNi phase diagram (where no FCC phase appears). Therefore, it is necessary to additionally calculate the degrees of SRO developed at 900 °C and 1200 °C.

We next revisited Zhu and Wu's work [50] by performing DFT-MC simulations (see Section 2.5) at 900 °C and 1200 °C, respectively, to yield corresponding degrees of SRO, as shown in **Fig. S1**. The rapid development of SRO at 900 °C (**Fig. S1(c)**) and 1200 °C (**Fig. S1(d)**) can be understood by the strong disfavoring and favoring V-V pairs at 1NN (α^1_{VV}) and 2NN (α^2_{VV}), respectively. More notably, α^2_{VV} of the A900 alloy (− 1.01) is much more negative than that of the A1200 alloy (− 0.64), suggesting a higher SRO tendency in the A900 alloy. This can be further quantitatively confirmed by the larger value of the SRO degree ($\sum_{ij,s}\left|\alpha^{s}_{ij}{}^{\leq 2}\right|$) at 900 °C, *i.e.*, 4.33 for the A900 alloy and 3.63 for the A1200 alloy. The SRO degrees of two alloys can be expressed in terms of SFE by using the classical pair-interaction model. It has been shown that the SFE change between the SRO and SQS states ($SFE^{SRO} - SFE^{SQS}$) is linearly proportional to the SRO degree, and SFE^{SQS} is 19 mJ/m^2 [50]. Considering that such linear scaling should be materials-dependent, we only extracted the VCoNi data points from Fig. 9(b) of *ref.* 50 for the present linear fitting, as shown in Fig. 11**(b)**. Additionally, we found that the SRO degree of the SQS structure is 0.64 rather than ideally 0 due to the size limitation of the DFT calculation. To optimize the fitting analysis [50], the SFE change between the SRO and random states ($SFE^{SRO} - SFE^{random}$) plotting with the SRO degree (Fig. 11**(b)**) was adopted instead, and SFE^{random} was estimated to be−35 mJ/m^2 when $\sum_{ij,s}\left|\alpha^{s}_{ij}\right| =$ 0, as shown in **Fig. S13**. Then, by substituting our MC-simulated SRO degrees at 900 °C and 1200 °C−4.33 and 3.63, respectively, into the fitting line, the corresponding SFE changes could be derived, as shown in Fig. 11**(b)**. As a result, the predicted mean SFEs at 900 and 1200 °C are 222 and 180 mJ/m^2, respectively.

The exceptionally high SFE of 222 mJ/m^2 with a narrow partial separation of 0.88 nm at 900 °C is consistent with the experimental observations, demonstrating that SRO is well developed in the A900 alloy. Although the DFT-MC simulation overrates the SFE of the A1200 alloy, the experimental and theoretical agreements on the decreasing trend in SFE from 900 to 1200 °C proved that the pronounced SROs can be thermodynamically stable at intermediate temperatures but gradually dissolve into the matrix with increasing temperatures. Similar peak-aging conditions were also reported in the CrCoNi MEA [19,27,29]. Accordingly, it is expected that the SFE could approach the value in the SQS or random state (even lower than that of the A1200 alloy) if the SRO could eventually dissipate at higher annealing temperatures.

Combined with the reasoning of the way SFE was affected by SRO, we schematically illustrated how SRO intervened in dislocation movements to sum up the above discussions. Fig. 11**(c)** shows partial dislocations gliding in the pure FCC metal, A1200, and A900 alloys (in ascending order of SRO degrees). Typically, smooth partial dislocations with a slight variation in the SF width can be found in the pure FCC metal without suspecting SRO. In contrast, wavy partial dislocations with significant SF width (or SFE) variations are expected in the A1200 alloy due to the locally developed SRO, which explains the contradiction between computations and experiments in forming DTs. With the increase of the SRO degree, high-density SRO domains are evenly distributed over the A900 alloy, resulting in frequently but slightly fluctuated partial dislocations with a restricted partial separation (high SFE) and a minor variation in the SF width. Even though the A900 alloy

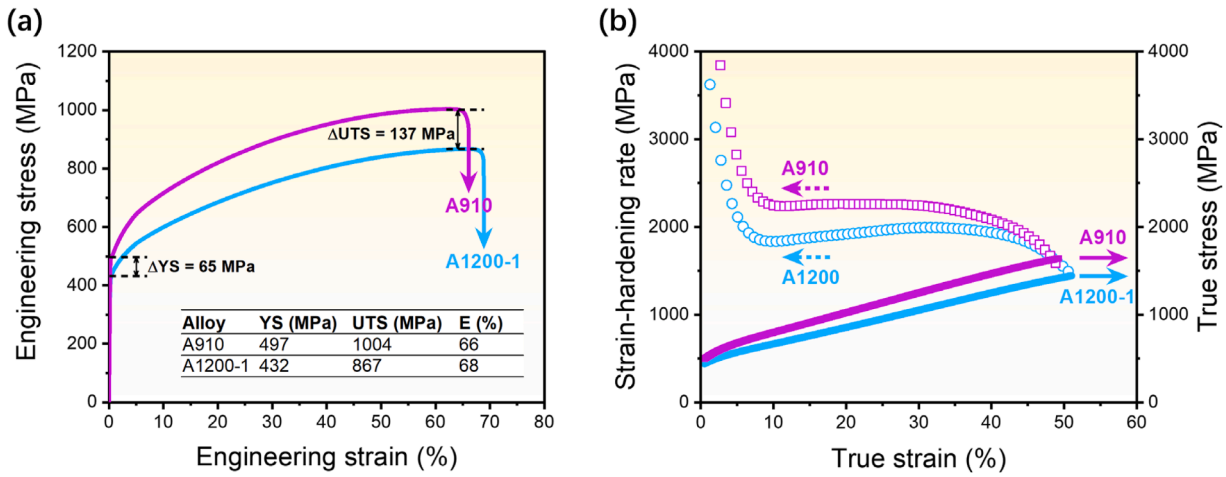

Fig. 12. Evaluation of SRO strengthening. (a) Engineering stress-strain curves of the A910 and A1200-1 alloys, including values of yield stress (YS), ultimate tensile stress (UTS), and elongation (E) summarized in the inset table. (b) True stress-strain curves and the corresponding strain-hardening rates of the A910 and A1200-1 alloys. The mean grain sizes of the A910 and A1200-1 alloys are ~ 64 μm and ~ 61 μm, respectively.

has a narrow range of variation in the SF width (as the pure FCC metal does), its local SFE could vary widely and comparably to the A1200 alloy. On average, the lower global SFE makes slip planarity preside over the deformation mechanism in the A1200 alloy (Fig. 6).

Lastly, additional tensile tests were conducted to evaluate SRO strengthening. To rule out the influences of precipitation strengthening (minor κ phase at grain boundaries of the A900 alloy (Fig. 3**(a)**) and grain boundary strengthening (difference between the mean grain sizes of the A900 (~ 64 μm) and A1200 (~ 122 μm) alloys) on the mechanical properties, the single-phase A910 alloy with a mean grain size of ~ 64 μm (**Fig. S8(d)**) was selected in comparison to the specimen with a similar mean grain size of ~ 61 μm (fabricated by cold rolling and then annealing at 1200 °C for 5 min; referred to as A1200-1). Fig. 12**(a)** displays the engineering stress-strain curves of the A910 and A1200-1 alloys. By comparison, both alloys have similar ductility, but the yield strength and ultimate tensile strength of the A910 alloy are 65 MPa and 137 MPa, respectively, higher than those of the A1200-1 alloy. Namely, SRO strengthening could contribute ~ 15 % increase to the yield strength and ultimate tensile strength without sacrificing ductility. Besides, it can be seen that the mechanical properties of the A910 closely resemble that of the A900 alloy (Fig. 4**(a)**), indicating that the minor κ phase with a volume fraction of 5 % has less influence on the deformation of the A900 alloy. Moreover, the corresponding true stress-strain curves and strain-hardening rates of the A910 and A1200-1 alloys were

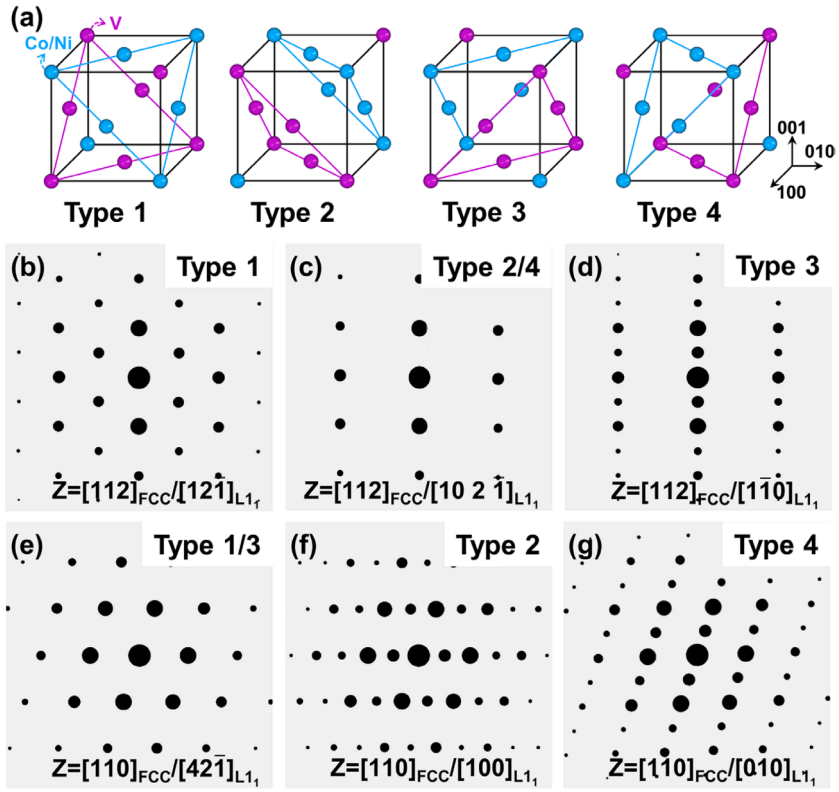

Fig. 13. Theoretical construction of $L1_1$ ordering. (a) Schematic illustration of four $L1_1$ variants in the FCC coordinate system with the corresponding simulated SAED patterns along (b)–(d) [112] and (e)–(g) [110] zone axes.

provided for comparing deformation mechanisms, as shown in Fig. 12 **(b)**. Still, within the true strain ranging from 10 % to 30 %, an upward trend in the strain-hardening rate can be only revealed in the A1200-1 alloy, similar to that in the A1200 alloy (Fig. 4**(b)**). This upturn in the strain hardening rate is commonly featured by SF/DT/phase transformation-mediated deformation mechanisms of alloys with low or medium SFE [86–89], reinforcing the evidence that the VCoNi alloy has a lower SFE at 1200 °C.

Overall, it is our conclusion that SRO indeed has impacts on deformation mechanisms and mechanical properties to varying degrees. Meanwhile, we also concur that solely relying on SRO strengthening may not be an efficient strategy to pursue high-performance alloys [26], as its present contribution to the entire strength is somewhat limited in both VCoNi and CrCoNi alloys [19,27–29]. Considering SRO strengthening could be highly material-dependent, its role in other alloy systems should be carefully evaluated and discussed case-by-case. Nevertheless, SRO-relevant issues remain of scientific interest, especially for explorations of SRO-affected physical properties (in addition to electrical resistance and SFE), precise expressions of SRO through simulation methods, and effective strategies to characterize the SRO.

4.4. *On the validity of characterizing SRO by only using the electron diffraction method*

Electron diffraction, as one of the most attainable methods to examine the existence of SRO, has been extensively employed since the SRO was reported in the VCoNi [24,37] and CrCoNi alloys [21,27]. Chen et al. ascribed additional diffuse intensities at 1/2{311} superlattice positions along the [112] zone axis to the SRO in the FCC VCoNi alloy [24], which was subsequently framed by the $L1_1$ (CuPt) structure [37]. Accordingly, we revisited this explanation with further comprehensive considerations.

First, the theoretical SRO structure and corresponding SAED patterns are constructed. In the FCC coordinate system, the $L1_1$ ordering (R-3 m rhombohedral structure with $\alpha = \beta = 90°$ and $\gamma = 120°$) can be equivalently understood by V-rich and Co/Ni-rich {111} planes alternately stacking along [111] (type 1), [$\bar{1}$11] (type 2), [$\bar{1}\bar{1}$1] (type 3), and [1$\bar{1}$1] (type 4), as shown in Fig. 13**(a)**. The simulated SAED patterns of these four types along [112] and [110] are presented in Fig. 13**(b)–(d)** and Fig. 13**(e)–(g)**, respectively. Then, to inspect possible reflections of the VCoNi alloy along [112], Fig. 14**(a)** schematically illustrates the corresponding FCC lattice, including four types of $L1_1$ variants. It can be seen that type 1 and type 3 are expected to produce additional reflections, *i.e.*, the 1/2{311} (Fig. 13**(b)**) and 1/2{111} (Fig. 13**(d)**), respectively, while type 2 and type 4 (consisting of mixed atom columns in the [112] direction) result in intensities identical to that of FCC solid solution (Fig. 13**(c)**) [30]. However, as previous investigations did, we only observed 1/2{311} diffuse disks in the SAED patterns (along the [112] zone axes of the FCC grains) of the A900 (Fig. 14**(b)**) and A1200 alloys (Fig. 14**(c)**). In the same way, the $L1_1$ ordering in the VCoNi alloy along [110] can also be discussed. In the schematically illustrated FCC lattice (Fig. 14**(d)**), only type 2 and type 4 can give rise to additional reflections, *i.e.*, the 1/2{111} (Fig. 13**(f)** and Fig. 13**(g)**), in this direction, which were still missing in the experimental SAED patterns (along the

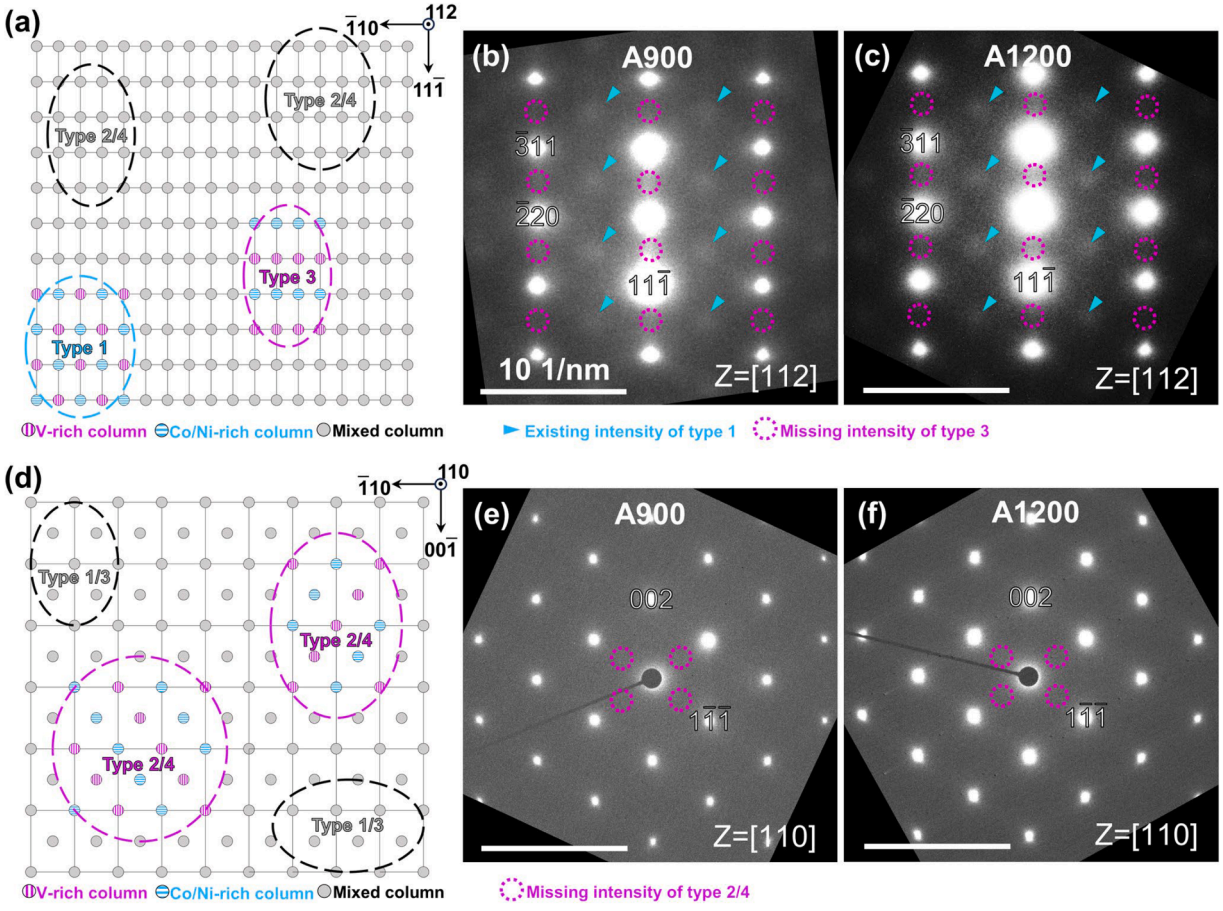

Fig. 14. Examination into the validity of characterizing SRO using the electron diffraction approach. (a) Schematic illustration of the FCC lattices including four types of $L1_1$ variants observed from the [112] direction. Experimental SAED patterns of the (b) A900 and (c) A1200 alloys taken along the [112] zone axis. (d) Schematic illustration of the FCC lattice, including four $L1_1$ variants observed from the [110] direction. Experimental SAED patterns of the (e) A900 and (f) A1200 alloys taken along the [110] zone axis.

[110] zone axes of the FCC grains) of the A900 (Fig. 14**(e)**) and A1200 alloys (Fig. 14**(f)**). Apparently, the missing reflections do not support the premise that SRO can be detected by using the electron diffraction approach. The existing diffuse disks at 1/2{311} along the [112] zone axis may be determined as reflections from higher-order Laue zones instead [31].

Consequently, further evidence of atomic-resolution EDS mapping combined with SAED patterns should be interpreted carefully as well. This is not only because of the flaw in reasoning using electron diffraction but also the oversight of the TEM sample thickness relative to the size of SRO, as recently concerned by the TEM community [10,19,30,31,90]. It should be emphasized that every single atom in the STEM image actually represents a column of atoms, and the effective length of a column, *i.e.*, the length of electron channeling, is mainly determined by the wavelength and convergent angle of the electron beam [91]. For the regular operation of EDS in the conventional Cs-corrected STEM, such channeling length could range from 5 to 30 nm, which is 10 to 50 times larger than the asserted size of the SRO (~ 0.6 nm) [24], as illustrated in **Fig. S14**. Under this circumstance, it is challenging to differentiate the SRO from the matrix due to the mixed intensity along the atomic column unless the sample thickness could be significantly reduced. Nevertheless, this incapability calls for future advancement in characterizing the SRO, such as the data-driven electron diffraction using 4D-STEM [92], machine-learning-enhanced APT [90], and atomic electron tomography [93].

5. Conclusion

In this study, we thoroughly investigated the phase stability of the equiatomic VCoNi MEA by conducting long-term annealing at medium to high temperatures, and thus resolved increasing disputes on critical temperatures for phase transitions, deformation mechanisms, crystal structures of phases, and the validity of characterizing SRO by using electron diffraction. Moreover, a new insight into the correlation between SFE and SRO was experimentally and computationally provided. The key achievements can be drawn as follows.

(i) The overall microstructural evolutions can be understood by a near hypoeutectoid reaction. Two intermetallic phases, κ and σ, tend to be stabilized at low temperatures. With rising annealing temperature, the κ + σ → FCC transformation will take place at a temperature close to 860 °C and end before 870 °C, resulting in an FCC + κ structure. The remaining κ phase will continuously dissolve into the FCC matrix until the critical temperature for a single-phase solid solution is reached (~ 910 °C). Therefore, it is recommended to exercise additional caution when investigating the SRO or mechanical properties of the VCoNi alloy, if a single FCC structure is obtained through short-term annealing at or below 900 °C.

(ii) The κ and σ phases were analyzed at the atomic level using the HAADF-STEM. Within the κ phase, a κ-approximant was discovered, which exhibited additional chemical order and could explain the off-stoichiometric compositions of the κ phase. The κ phase was also found to accommodate considerable plastic deformation by activating the $\langle c+a \rangle$ slip systems. Furthermore, it was proved that the σ phase in the VCoNi alloy is of the $Cr_{49.5}Fe_{50.5}$ type, rather than the previously reported $V_{62}Co_{38}$ type.

(iii) Experimental measurements of SF widths combined with the DFT-MC simulation suggest that SFE may increase with a greater degree of SRO, which could further affect the deformation mechanism such as slip planarity and strain-hardening rate. Significant variations in the local SFE induced by SRO were unveiled to elucidate the dislocation dissociation (into partial dislocations) and the absence of DT.

(iv) SRO has but limited effects on the mechanical properties of the VCoNi alloy with only ~ 15 % increase in the yield strength and ultimate tensile strength, similar to that in the CrCoNi alloy [19,27–29]. In view of this trend, SRO strengthening may not be an efficient strategy to greatly improve the mechanical performance of this type of alloys. Still, such a material-dependent effect should be carefully evaluated on a case-by-case basis.

(v) Additional superlattice intensities in reciprocal space could be recognized as specific orderings on the premise that SRO can be detected using electron diffraction. However, combined with simulations and atomic arrangements, neither $L1_1$ nor other orderings could be identified in the obtained SAED patterns along the [112] and [110] zone axes of the VCoNi alloy. The observed diffuse disks at 1/2{311} of the [112] zone axes cannot unambiguously stand for $L1_1$ ordering. Future development of advanced techniques to characterize SRO is still needed.

CRediT authorship contribution statement

T.H. Chou: Writing – original draft, Methodology, Investigation, Formal analysis, Data curation. **W.P. Li:** Writing – review & editing, Writing – original draft, Validation, Methodology, Investigation, Formal analysis, Data curation, Conceptualization. **L.Y. Zhu:** Software, Methodology, Investigation, Data curation. **F. Zhu:** Investigation. **X.C. Li:** Investigation. **J. Huang:** Investigation. **Y.X. Wang:** Investigation. **R. Zhou:** Investigation. **W.Y. Chen:** Investigation. **J.H. Luan:** Investigation. **Y.L. Zhao:** Writing – review & editing, Resources. **Z.X. Wu:** Writing – review & editing, Resources. **F.R. Chen:** Writing – review & editing, Supervision, Resources. **J.C. Huang:** Writing – review & editing. **P.K. Liaw:** Writing – review & editing. **X.L. Wang:** Writing – review & editing. **T. Yang:** Writing – review & editing, Supervision, Conceptualization.

Declaration of competing interest

The authors declare that they have no known competing financial interests or personal relationships that could have appeared to influence the work reported in this paper.

Acknowledgement

The authors greatly acknowledge the financial support from the National Key R & D Program of China (No. 2022YFE0200900) and Hong Kong Research Grant Council (RGC) (Grant No. C1020-21G). P.K. Liaw very much appreciates the support from the National Science Foundation (DMR-1611180, 1809640, and 2226508) and the Army Research Office (W911NF-13-1-0438 and W911NF-19-2-0049). X.L. Wang thanks the Croucher Foundation for the Croucher Senior Research Fellowship (CityU 9509008). APT research was conducted at the Inter-University 3D APT Unit of City University of Hong Kong (CityU), supported by the grant 9360161.

Supplementary materials

Supplementary material associated with this article can be found, in the online version, at doi:10.1016/j.actamat.2024.120190.

References

[1] D.B. Miracle, O.N. Senkov, A critical review of high entropy alloys and related concepts, Acta Mater. 122 (2017) 448–511.
[2] Z. Li, S. Zhao, R.O. Ritchie, M.A. Meyers, Mechanical properties of high-entropy alloys with emphasis on face-centered cubic alloys, Prog. Mater. Sci. 102 (2019) 296–345.
[3] E.P. George, D. Raabe, R.O. Ritchie, High-entropy alloys, Nat. Rev. Mater. 4 (2019) 515–534.

[4] E.P. George, W. Curtin, C.C. Tasan, High entropy alloys: a focused review of mechanical properties and deformation mechanisms, Acta Mater. 188 (2020) 435–474.
[5] N.K. Katiyar, K. Biswas, J.W. Yeh, S. Sharma, C.S. Tiwary, A perspective on the catalysis using the high entropy alloys, Nano Energy 88 (2021) 106261.
[6] F. Marques, M. Balcerzak, F. Winkelmann, G. Zepon, M. Felderhoff, Review and outlook on high-entropy alloys for hydrogen storage, Energy Environ. Sci. 14 (2021) 5191–5227.
[7] J.W. Yeh, S.K. Chen, S.J. Lin, J.Y. Gan, T.S. Chin, T.T. Shun, C.H. Tsau, S.Y. Chang, Nanostructured high-entropy alloys with multiple principal elements: novel alloy design concepts and outcomes, Adv. Eng. Mater. 6 (2004) 299–303.
[8] J.W. Yeh, Recent progress in high entropy alloys, Ann. Chim. Sci. Mat. 31 (2006) 633–648.
[9] W. Steurer, Single-phase high-entropy alloys–A critical update, Mater. Charact. 162 (2020) 110179.
[10] R. Zhang, Y. Chen, Y. Fang, Q. Yu, Characterization of chemical local ordering and heterogeneity in high-entropy alloys, MRS Bull. 47 (2022) 186–193.
[11] F. Walsh, A. Abu-Odeh, M. Asta, Reconsidering short-range order in complex concentrated alloys, MRS Bull. 48 (2023) 753–761.
[12] B. Schuh, F. Mendez-Martin, B. Völker, E.P. George, H. Clemens, R. Pippan, A. Hohenwarter, Mechanical properties, microstructure and thermal stability of a nanocrystalline CoCrFeMnNi high-entropy alloy after severe plastic deformation, Acta Mater. 96 (2015) 258–268.
[13] E. Pickering, R. Muñoz-Moreno, H. Stone, N. Jones, Precipitation in the equiatomic high-entropy alloy CrMnFeCoNi, Scr. Mater. 113 (2016) 106–109.
[14] F. Otto, A. Dlouhý, K.G. Pradeep, M. Kuběnová, D. Raabe, G. Eggeler, E.P. George, Decomposition of the single-phase high-entropy alloy CrMnFeCoNi after prolonged anneals at intermediate temperatures, Acta Mater. 112 (2016) 40–52.
[15] T.H. Chou, J.C. Huang, C.H. Yang, S.K. Lin, T.G. Nieh, Consideration of kinetics on intermetallics formation in solid-solution high entropy alloys, Acta Mater. 195 (2020) 71–80.
[16] A. Tamm, A. Aabloo, M. Klintenberg, M. Stocks, A. Caro, Atomic-scale properties of Ni-based FCC ternary, and quaternary alloys, Acta Mater. 99 (2015) 307–312.
[17] F. Zhang, S. Zhao, K. Jin, H. Xue, G. Velisa, H. Bei, R. Huang, J. Ko, D. Pagan, J. Neuefeind, Local structure and short-range order in a NiCoCr solid solution alloy, Phys. Rev. Lett. 118 (2017) 205501.
[18] J. Ding, Q. Yu, M. Asta, R.O. Ritchie, Tunable stacking fault energies by tailoring local chemical order in CrCoNi medium-entropy alloys, Proc. Natl. Acad. Sci. 115 (2018) 8919–8924.
[19] R. Zhang, S. Zhao, J. Ding, Y. Chong, T. Jia, C. Ophus, M. Asta, R.O. Ritchie, A. M. Minor, Short-range order and its impact on the CrCoNi medium-entropy alloy, Nature 581 (2020) 283–287.
[20] J. Wang, P. Jiang, F. Yuan, X. Wu, Chemical medium-range order in a medium-entropy alloy, Nat. Commun. 13 (2022) 1021.
[21] L. Zhou, Q. Wang, J. Wang, X. Chen, P. Jiang, H. Zhou, F. Yuan, X. Wu, Z. Cheng, E. Ma, Atomic-scale evidence of chemical short-range order in CrCoNi medium-entropy alloy, Acta Mater. 224 (2022) 117490.
[22] Y. Ma, Q. Wang, C. Li, L.J. Santodonato, M. Feygenson, C. Dong, P.K. Liaw, Chemical short-range orders and the induced structural transition in high-entropy alloys, Scr. Mater. 144 (2018) 64–68.
[23] E. Antillon, C. Woodward, S. Rao, B. Akdim, T. Parthasarathy, Chemical short range order strengthening in a model FCC high entropy alloy, Acta Mater. 190 (2020) 29–42.
[24] X. Chen, Q. Wang, Z. Cheng, M. Zhu, H. Zhou, P. Jiang, L. Zhou, Q. Xue, F. Yuan, J. Zhu, Direct observation of chemical short-range order in a medium-entropy alloy, Nature 592 (2021) 712–716.
[25] E. Antillon, C. Woodward, S. Rao, B. Akdim, Chemical short range order strengthening in BCC complex concentrated alloys, Acta Mater. 215 (2021) 117012.
[26] B. Yin, S. Yoshida, N. Tsuji, W. Curtin, Yield strength and misfit volumes of NiCoCr and implications for short-range-order, Nat. Commun. 11 (2020) 2507.
[27] M. Zhang, Q. Yu, C. Frey, F. Walsh, M.I. Payne, P. Kumar, D. Liu, T.M. Pollock, M. D. Asta, R.O. Ritchie, Determination of peak ordering in the CrCoNi medium-entropy alloy via nanoindentation, Acta Mater. 241 (2022) 118380.
[28] K. Inoue, S. Yoshida, N. Tsuji, Direct observation of local chemical ordering in a few nanometer range in CoCrNi medium-entropy alloy by atom probe tomography and its impact on mechanical properties, Phys. Rev. Mater. 5 (2021) 085007.
[29] L. Li, Z. Chen, S. Kuroiwa, M. Ito, K. Yuge, K. Kishida, H. Tanimoto, Y. Yu, H. Inui, E.P. George, Evolution of short-range order and its effects on the plastic deformation behavior of single crystals of the equiatomic Cr-Co-Ni medium-entropy alloy, Acta Mater. 243 (2023) 118537.
[30] F. Walsh, M. Zhang, R.O. Ritchie, A.M. Minor, M. Asta, Extra electron reflections in concentrated alloys do not necessitate short-range order, Nat. Mater. 22 (2023) 926–929.
[31] F.G. Coury, C. Miller, R. Field, M. Kaufman, On the origin of diffuse intensities in fcc electron diffraction patterns, Nature 622 (2023) 742–747.
[32] B. Schönfeld, Local atomic arrangements in binary alloys, Prog. Mater. Sci. 44 (1999) 435–543.
[33] J.P. Chevalier, W. Stobbs, An electron diffraction study of short-range order in quenched Ni4Mo alloy, Acta Metall. 24 (1976) 535–542.
[34] W. Pfeiler, Investigation of short-range order by electrical resistivity measurement, Acta Metall. 36 (1988) 2417–2434.
[35] B. Schönfeld, C.R. Sax, J. Zemp, M. Engelke, P. Boesecke, T. Kresse, T. Boll, T.a. Al-Kassab, O.E. Peil, A.V. Ruban, Local order in Cr-Fe-Co-Ni: experiment and electronic structure calculations, Phys. Rev. B 99 (2019) 014206.
[36] A. Fantin, G.O. Lepore, A.M. Manzoni, S. Kasatikov, T. Scherb, T. Huthwelker, F. d'Acapito, G. Schumacher, Short-range chemical order and local lattice distortion in a compositionally complex alloy, Acta Mater. 193 (2020) 329–337.
[37] X. Chen, F. Yuan, H. Zhou, X. Wu, Structure motif of chemical short-range order in a medium-entropy alloy, Mater. Res. Lett. 10 (2022) 149–155.
[38] Z. Su, T. Shi, H. Shen, L. Jiang, L. Wu, M. Song, Z. Li, S. Wang, C. Lu, Radiation-assisted chemical short-range order formation in high-entropy alloys, Scr. Mater. 212 (2022) 114547.
[39] J.B. Seol, W.-S. Ko, S.S. Sohn, M.Y. Na, H.J. Chang, Y.U. Heo, J.G. Kim, H. Sung, Z. Li, E. Pereloma, Mechanically derived short-range order and its impact on the multi-principal-element alloys, Nat. Commun. 13 (2022) 6766.
[40] D. Zhou, Z. Chen, K. Ehara, K. Nitsu, K. Tanaka, H. Inui, Effects of annealing on hardness, yield strength and dislocation structure in single crystals of the equiatomic Cr-Mn-Fe-Co-Ni high entropy alloy, Scr. Mater. 191 (2021) 173–178.
[41] M. Kawamura, M. Asakura, N.L. Okamoto, K. Kishida, H. Inui, E.P. George, Plastic deformation of single crystals of the equiatomic Cr−Mn−Fe−Co−Ni high-entropy alloy in tension and compression from 10 K to 1273 K, Acta Mater. 203 (2021) 116454.
[42] Q. Ding, Y. Zhang, X. Chen, X. Fu, D. Chen, S. Chen, L. Gu, F. Wei, H. Bei, Y. Gao, M. Wen, J. Li, Z. Zhang, T. Zhu, R.O. Ritchie, Q. Yu, Tuning element distribution, structure and properties by composition in high-entropy alloys, Nature 574 (2019) 223–227.
[43] Y.H. Zhang, Y. Zhuang, A. Hu, J.J. Kai, C.T. Liu, The origin of negative stacking fault energies and nano-twin formation in face-centered cubic high entropy alloys, Scr. Mater. 130 (2017) 96–99.
[44] S. Zhao, G.M. Stocks, Y. Zhang, Stacking fault energies of face-centered cubic concentrated solid solution alloys, Acta Mater. 134 (2017) 334–345.
[45] H. Huang, X. Li, Z. Dong, W. Li, S. Huang, D. Meng, X. Lai, T. Liu, S. Zhu, L. Vitos, Critical stress for twinning nucleation in CrCoNi-based medium and high entropy alloys, Acta Mater. 149 (2018) 388–396.
[46] Z. Pei, S. Zhang, Y. Lei, F. Zhang, M. Chen, Decoupling between Shockley partials and stacking faults strengthens multiprincipal element alloys, Proc. Natl. Acad. Sci. 118 (2021) e2114167118.
[47] G. Laplanche, A. Kostka, C. Reinhart, J. Hunfeld, G. Eggeler, E. George, Reasons for the superior mechanical properties of medium-entropy CrCoNi compared to high-entropy CrMnFeCoNi, Acta Mater. 128 (2017) 292–303.
[48] S. Liu, Y. Wu, H. Wang, J. He, J. Liu, C. Chen, X. Liu, H. Wang, Z. Lu, Stacking fault energy of face-centered-cubic high entropy alloys, Intermetallics 93 (2018) 269–273.
[49] T.M. Smith, M.S. Hooshmand, B.D. Esser, F. Otto, D.W. McComb, E.P. George, M. Ghazisaeidi, M.J. Mills, Atomic-scale characterization and modeling of 60 dislocations in a high-entropy alloy, Acta Mater. 110 (2016) 352–363.
[50] L. Zhu, Z. Wu, Effects of short range ordering on the generalized stacking fault energy and deformation mechanisms in FCC multiprincipal element alloys, Acta Mater. 259 (2023) 119230.
[51] T. Kostiuchenko, A.V. Ruban, J. Neugebauer, A. Shapeev, F. Körmann, Short-range order in face-centered cubic VCoNi alloys, Phys. Rev. Mater. 4 (2020) 113802.
[52] S.S. Sohn, A. Kwiatkowski da Silva, Y. Ikeda, F. Körmann, W. Lu, W.S. Choi, B. Gault, D. Ponge, J. Neugebauer, D. Raabe, Ultra strong medium-entropy single-phase alloys designed via severe lattice distortion, Adv. Mater. 31 (2019) 1807142.
[53] H. Luo, S.S. Sohn, W. Lu, L. Li, X. Li, C.K. Soundararajan, W. Krieger, Z. Li, D. Raabe, A strong and ductile medium-entropy alloy resists hydrogen embrittlement and corrosion, Nat. Commun. 11 (2020) 3081.
[54] S.S. Sohn, D.G. Kim, Y.H. Jo, A.K. da Silva, W. Lu, A.J. Breen, B. Gault, D. Ponge, High-rate superplasticity in an equiatomic medium-entropy VCoNi alloy enabled through dynamic recrystallization of a duplex microstructure of ordered phases, Acta Mater. 194 (2020) 106–117.
[55] J.M. Park, D.C. Yang, H.J. Kim, D.G. Kim, S. Lee, H.S. Kim, S.S. Sohn, Ultra-strong and strain-hardenable ultrafine-grained medium-entropy alloy via enhanced grain-boundary strengthening, Mater. Res. Lett. 9 (2021) 315–321.
[56] D.C. Yang, Y.H. Jo, Y. Ikeda, F. Körmann, S.S. Sohn, Effects of cryogenic temperature on tensile and impact properties in a medium-entropy VCoNi alloy, J. Mater. Sci. Technol. 90 (2021) 159–167.
[57] R.K. Nutor, T. Xu, X. Wang, X.D. Wang, P. An, J. Zhang, T. Hu, L. Li, Q. Cao, S. Ding, Liquid helium temperature deformation and local atomic structure of CoNiV medium entropy alloy, Mater. Today Commun. 30 (2022) 103141.
[58] F. An, J. Hou, J. Liu, B. Qian, W. Lu, Deformable κ phase induced deformation twins in a CoNiV medium entropy alloy, Int. J. Plasticity 160 (2023) 103509.
[59] R. Kilaas, Optimal and near-optimal filters in high-resolution electron microscopy, J. Microsc. 190 (1998) 45–51.
[60] M. Hÿtch, E. Snoeck, R. Kilaas, Quantitative measurement of displacement and strain fields from HREM micrographs, Ultramicroscopy 74 (1998) 131–146.
[61] C.T. Koch, Determination of Core Structure Periodicity and Point Defect Density Along Dislocations, Arizona State University, 2002.
[62] G. Kresse, J. Hafner, Ab initio molecular dynamics for liquid metals, Phys. Rev. B 47 (1993) 558.
[63] G. Kresse, J. Furthmüller, Efficient iterative schemes for ab initio total-energy calculations using a plane-wave basis set, Phys. Rev. B 54 (1996) 11169.
[64] J.P. Perdew, K. Burke, M. Ernzerhof, Generalized gradient approximation made simple, Phys. Rev. Lett. 77 (1996) 3865.
[65] P.E. Blöchl, Projector augmented-wave method, Phys. Rev. B 50 (1994) 17953.
[66] A. Zunger, S.-H. Wei, L. Ferreira, J.E. Bernard, Special quasirandom structures, Phys. Rev. Lett. 65 (1990) 353.
[67] A. Van de Walle, P. Tiwary, M. De Jong, D. Olmsted, M. Asta, A. Dick, D. Shin, Y. Wang, L.Q. Chen, Z.K. Liu, Efficient stochastic generation of special quasirandom structures, CALPHAD 42 (2013) 13–18.

[68] W.K. Hastings, Monte Carlo sampling methods using Markov chains and their applications, Biometrika 57 (1970) 97–109.
[69] C.T. Liu, Atomic ordering and structural transformation in the V-Co-Ni ternary alloys, Metall. Trans. 4 (1973) 1743–1753.
[70] C.T. Liu, Physical metallurgy and mechanical properties of ductile ordered alloys (Fe, Co, Ni)$_3$V, Int. Metals Rev. 29 (1984) 168–194.
[71] T. Onozuka, S. Yamaguchi, M. Hirabayashi, Long-period ordered structures in the quasi-binary Co_3V–Ni_3V alloy, J. Appl. Crystallogr. 6 (1973) 273–279.
[72] J.M. De Freitas, L.A. da Veiga, W. Gonschorek, The ordering of the sigma phase V62 Co38, Portug. Phys. 13 (1982) 117.
[73] A. Sinha, Close-packed ordered AB_3 structures in ternary alloys of certain transition metals, Trans. Met. Soc. AIME 245 (1969) 911–917.
[74] D.A. Porter, K.E. Easterling, M.Y. Sherif, Phase Transformations in Metals and Alloys, CRC Press, 2021.
[75] H. Gardner, S. Pedrazzini, J.O. Douglas, D. De Lille, M.P. Moody, P.A. Bagot, Atom probe tomography investigations of microstructural evolution in an aged nickel superalloy for exhaust applications, Metall. Mater. Trans. A 50 (2019) 1862–1872.
[76] D. Collins, L. Yan, E. Marquis, L. Connor, J. Ciardiello, A. Evans, H. Stone, Lattice misfit during ageing of a polycrystalline nickel-base superalloy, Acta Mater. 61 (2013) 7791–7804.
[77] K. Hagihara, T. Tanaka, T. Nakano, P. Veyssière, Y. Umakoshi, Effects of the anisotropy of the anti-phase boundary energy on the yield-stress anomaly in Ni_3X compounds with close-packed crystal structures, Philos. Mag. Lett. 87 (2007) 705–712.
[78] K. Hagihara, T. Tanaka, H. Izuno, Y. Umakoshi, T. Nakano, Non-basal slip in Ni_3(Ti, Nb) and Ni_3(Ti, Al) single crystals with various long-period stacking ordered structures, Acta Mater. 61 (2013) 4365–4373.
[79] X. Xu, P. Liu, Z. Tang, A. Hirata, S. Song, T. Nieh, P. Liaw, C. Liu, M. Chen, Transmission electron microscopy characterization of dislocation structure in a face-centered cubic high-entropy alloy $Al_{0.1}$CoCrFeNi, Acta Mater. 144 (2018) 107–115.
[80] P. Hartel, H. Rose, C. Dinges, Conditions and reasons for incoherent imaging in STEM, Ultramicroscopy 63 (1996) 93–114.
[81] J.W. Cahn, On spinodal decomposition, Acta Metall. 9 (1961) 795–801.
[82] A. Orthacker, G. Haberfehlner, J. Taendl, M.C. Poletti, B. Sonderegger, G. Kothleitner, Diffusion-defining atomic-scale spinodal decomposition within nanoprecipitates, Nat. Mater. 17 (2018) 1101–1107.
[83] J.M. Joubert, Crystal chemistry and Calphad modeling of the σ phase, Prog. Mater. Sci. 53 (2008) 528–583.
[84] H. Yakel, Atom distributions in sigma phases. I. Fe and Cr atom distributions in a binary sigma phase equilibrated at 1063, 1013 and 923 K, Acta Crystallogr. Section B: Struct. Sci. 39 (1983) 20–28.
[85] X. Sun, S. Lu, R. Xie, X. An, W. Li, T. Zhang, C. Liang, X. Ding, Y. Wang, H. Zhang, Can experiment determine the stacking fault energy of metastable alloys? Mater. Des. 199 (2021) 109396.
[86] D.T. Pierce, J.A. Jiménez, J. Bentley, D. Raabe, J.E. Wittig, The influence of stacking fault energy on the microstructural and strain-hardening evolution of Fe–Mn–Al–Si steels during tensile deformation, Acta Mater. 100 (2015) 178–190.
[87] T. Yang, Y. Zhao, Y. Tong, Z.B. Jiao, J. Wei, J.X. Cai, X.D. Han, D. Chen, A. Hu, J. J. Kai, K. Lu, Y. Liu, C.T. Liu, Multicomponent intermetallic nanoparticles and superb mechanical behaviors of complex alloys, Science 362 (6417) (2018) 933–937.
[88] T. Yang, Y. Zhao, J.H. Luan, B. Han, J. Wei, J.J. Kai, C.T. Liu, Nanoparticles-strengthened high-entropy alloys for cryogenic applications showing an exceptional strength-ductility synergy, Scr. Mater. 164 (2019) 30–35.
[89] J.Y. Zhang, T.H. Chou, Y.H. Zhou, J.H. Luan, Y.L. Zhao, T. Yang, Corrosion-resistant $L1_2$-strengthened high-entropy alloy with high strength and large ductility, Corros. Sci. 225 (2023) 111593.
[90] Y. Li, Y. Wei, Z. Wang, X. Liu, T. Colnaghi, L. Han, Z. Rao, X. Zhou, L. Huber, R. Dsouza, Quantitative three-dimensional imaging of chemical short-range order via machine learning enhanced atom probe tomography, Nat. Commun. 14 (2023) 7410.
[91] T. Kiguchi, Y. Yamaguchi, S. Tashiro, K. Sato, Effect of focal depth of HAADF-STEM imaging on the solute enriched layers in Mg alloys, Mater. Trans. 56 (2015) 1633–1638.
[92] H.W. Hsiao, R. Feng, H. Ni, K. An, J.D. Poplawsky, P.K. Liaw, J.M. Zuo, Data-driven electron-diffraction approach reveals local short-range ordering in CrCoNi with ordering effects, Nat. Commun. 13 (2022) 6651.
[93] S. Moniri, Y. Yang, J. Ding, Y. Yuan, J. Zhou, L. Yang, F. Zhu, Y. Liao, Y. Yao, L. Hu, P. Ercius, J. Miao, Three-dimensional atomic structure and local chemical order of medium- and high-entropy nanoalloys, Nature 624 (2023) 564–569.